

MULTI-LEVEL FINE-TUNING: CLOSING GENERALIZATION GAPS IN APPROXIMATION OF SOLUTION MAPS UNDER A LIMITED BUDGET FOR TRAINING DATA *

ZHIHAN LI[†], YUWEI FAN[‡], AND LEXING YING[§]

Abstract. In scientific machine learning, regression networks have been recently applied to approximate solution maps (e.g., potential-ground state map of Schrödinger equation). In this paper, we aim to reduce the generalization error without spending more time in generating training samples. However, to reduce the generalization error, the regression network needs to be fit on a large number of training samples (e.g., a collection of potential-ground state pairs). The training samples can be produced by running numerical solvers, which takes much time in many applications. In this paper, we aim to reduce the generalization error without spending more time in generating training samples. Inspired by few-shot learning techniques, we develop the Multi-Level Fine-Tuning algorithm by introducing levels of training: we first train the regression network on samples generated at the coarsest grid and then successively fine-tune the network on samples generated at finer grids. Within the same amount of time, numerical solvers generate more samples on coarse grids than on fine grids. We demonstrate a significant reduction of generalization error in numerical experiments on challenging problems with oscillations, discontinuities, or rough coefficients. Further analysis can be conducted in the Neural Tangent Kernel regime and we provide practical estimators to the generalization error. The number of training samples at different levels can be optimized for the smallest estimated generalization error under the constraint of budget for training data. The optimized distribution of budget over levels provides practical guidance with theoretical insight as in the celebrated Multi-Level Monte Carlo algorithm.

Key words. multi-level method, few-shot learning, generalization, parametric model, neural tangent kernel

AMS subject classifications. 65N55, 65C20, 62J07, 68Q32

1. Introduction.

1.1. Background.

1.1.1. Approximating solution maps with regression networks. Contemporary machine learning techniques, especially deep neural networks, have been recently introduced to scientific computing tasks. For problems involving partial differential equations (PDEs), neural networks can be utilized as universal approximators to the solution function in order to solve a PDE directly [39, 51, 18, 34, 54]. In this setting, to solve the PDE $\mathcal{N}u = 0$ where \mathcal{N} is a differential operator and u is the solution function on domain $\Omega \subseteq \mathbb{R}^d$, one searches for a neural network NN which inputs the coordinate $\mathbf{x} \in \mathbb{R}^d$ and outputs an approximation to the solution function $\text{NN}(\mathbf{x}) \approx u(\mathbf{x})$. Another setting tackles the problem of parametric PDE $\mathcal{N}_v u_v = 0$ with variable parameter v (e.g., coefficients, initial values, source terms). In this setting, one may train a neural network to approximate the solution map $v \mapsto u_v$ (the parameter-solution map) in order to apply to various parameters [35]. For example,

*Submitted to the editors DATE.

Funding: Zhihan Li is partially supported by the elite undergraduate training program of the School of Mathematical Sciences at Peking University. Lexing Ying is partially supported by the National Science Foundation under award DMS-1818449 and by the U.S. Department of Energy, Office of Science, Office of Advanced Scientific Computing Research, Scientific Discovery through Advanced Computing (SciDAC) program.

[†]School of Mathematical Sciences, Peking University, Beijing 100871, China (zhli16@pku.edu.cn).

[‡]Department of Mathematics, Stanford University, Stanford, CA 94305 (ywfan1989@gmail.com).

[§]Department of Mathematics and Institute for Computational and Mathematical Engineering, Stanford University, Stanford, CA 94305 (lexing@stanford.edu).

we consider the one-dimensional non-linear Schrödinger equation on $\Omega = [0, 1]$ with a periodic boundary condition and a fixed dispersion coefficient $\beta > 0$ [8, 20]:

$$(1.1) \quad -\Delta u(x) + v(x)u(x) + \beta u^3(x) = Eu(x), \quad x \in [0, 1],$$

$$(1.2) \quad \int_{[0,1]} u^2(x) dx = 1, \quad \int_{[0,1]} u(x) dx > 0.$$

We are interested in the solution map from potential v (parameter) to ground state u_v (the function $u_v = u$ satisfying the equations with the smallest energy E , solution). Hence, we train a neural network which inputs potentials and outputs ground states to approximate the potential-ground state map $v \mapsto u_v$. Besides, in graphics, one may approximate the action of Poisson solver, namely the solution map of $-\Delta u_v = v$ from source term v (parameter) to u_v (solution) for faster Eulerian fluid simulation [59, 37]. For inverse problems, one may approximate the regularized inverse operator which maps observations (parameter) to reconstructions (solution) in a data-driven context [36, 7, 22, 23, 26]. Similar settings of approximating solution maps can also be seen in signal processing [58], molecular dynamics [62], model reduction [41], and operator compression [19, 20, 21].

In this paper, we focus on the setting of approximating solution maps. For discretization, one typically chooses a fine grid of interest (in contrast to the coarse grid introduced later) and discretizes the solution map as a fine-grid numerical solver. Since the fine grid can be chosen up to practical considerations, main problem of approximating the solution map is transformed into approximating the fine-grid solver. In order to harvest a neural network which approximates the fine-grid solver, one may fit a regression network (a neural network used as a regressor) on parameter-solution pairs generated by invoking the fine-grid solver. For example, in the non-linear Schrödinger equation problem, we independently sample a collection of potentials $\{v_m\}_{m=1}^M$ from a distribution \mathcal{D} as functions on grid with grid step $h = 1/320$. We then compute the corresponding ground states $u_m = u_{v_m}$ by running a gradient flow solver [9] on the grid. With the parameter-solution pairs $\{(v_m, u_m)\}_{m=1}^M$, we initialize and train a neural network NN to fit the training samples (v_m, u_m) .

1.1.2. Tradeoff between generalization and training data generation.

The error of regression network in approximating the fine-grid solver consists of two parts: (1) the training error on (v_m, u_m) and (2) the generalization error when applying the regression network on previously unseen samples (parameters) $v \sim \mathcal{D}$. In many cases, the neural network fits exactly at training samples because of over-parameterization [11, 42, 2], and hence the generalization error is of major concern.

The procedure described above to train a regression network lies in the framework of empirical risk minimization: we fit a statistical model (regression network) in a hypothesis space (e.g., functions representable by a neural network with bounded weights) by minimizing the empirical risk (training error) on training data, and then we evaluate the model on testing data in the hope of a low population risk (testing error). Generalization gap (generalization error) is the difference between the population risk and the empirical risk [46]. In particular, we have the following theorem bounding the generalization gap using Rademacher complexity [46].

THEOREM 1.1. *Let \mathcal{L} be a family of functions from a set \mathcal{V} to $[0, B]$ and $\{v_m\}_{m=1}^M$ be M independent random samples drawn from a distribution \mathcal{D} on \mathcal{V} . Then, for any positive δ , with probability at least $1 - \delta$ on sampling $\{v_m\}_{m=1}^M$, it holds for every*

$\ell \in \mathcal{L}$ that

$$(1.3) \quad \mathbb{E} \ell(v) - \hat{\mathbb{E}} \ell(v) \leq 2\hat{\mathfrak{R}}_v(\mathcal{L}) + 3B \sqrt{\frac{\log 1/\delta}{2M}}.$$

Here \mathcal{L} is the loss class (composition of statistical models and the loss function),

$$(1.4) \quad \mathbb{E} \ell(v) = \mathbb{E}_{v \sim \mathcal{D}} \ell(v), \quad \hat{\mathbb{E}} \ell(v) = \frac{1}{M} \sum_{m=1}^M \ell(v_m)$$

are the population risk and the empirical risk respectively, and

$$(1.5) \quad \hat{\mathfrak{R}}_v(\mathcal{L}) = \frac{1}{M} \mathbb{E}_\sigma \sup_{\ell \in \mathcal{L}} \sum_{m=1}^M \sigma_m \ell(v_m)$$

is the empirical Rademacher complexity, where σ_m are independent Bernoulli-like random variables which take the value ± 1 with equal probability.

Rademacher complexity delineates the complexity of hypothesis space and relates to the generalization gap. In various cases, $\hat{\mathfrak{R}}_v(\mathcal{L})$ decays in speed $O(1/\sqrt{M})$ (e.g., for linear class or kernel class [10, 16]). However, if M is small, the Rademacher complexity can be poorly bounded, and so can the generalization gap.

As a result, in order to accurately approximate the fine-grid solver (and the solution map), a sufficient number of training samples are in need. However, numerical solvers may suffer from heavy scaling laws in computational complexity with respect to grid step due to stability, convergence, or randomness issues. Hence, generating a large number of training samples with the fine-grid solver may take a long time. For example, in [22], it takes about 50 seconds to solve a radiative transfer equation when generating a single parameter-solution pair. As a result, the generation of the whole dataset, which consists of 10 240 samples of such pairs, takes days and turns out to be much slower and much more expensive than the training of regression network. We can observe the tradeoff between generalization and training data generation in this example. Hence, it comes the question whether it is possible to reduce the generalization error in approximating the fine-grid solver without spending more time in generating training samples. In other words, we aim to close the generalization gap under a limited budget for training data.

1.1.3. Multi-Level Fine-Tuning. Few-shot learning methods have been developed to mitigate the shortage of training samples. Prior knowledge is required to either augment training samples, reduce the hypothesis space, or reach a better parameterization [60]. One particularly popular method is fine-tuning, which was initially proposed for transfer learning tasks [60]. In this approach, a model is first fit on some other tasks called source tasks with a large amount of data. The model is then refined using a similar fitting procedure on a few-shot task called target task. The intermediate model, as a good starting point for the target task, contains some prior knowledge about the source tasks, which may be transferred to help the few-shot target task.

For image recognition tasks, models pre-trained on large-scale datasets like ImageNet [56] [30] serve as excellent starting points for fine-tuning. However, fine-grid numerical solvers to be approximated are problem-dependent. It is difficult to find a pre-trained model well-suited for multiple different problems in scientific machine learning. Meanwhile, according to multi-scale methods, we may capture rough shapes

of solutions on a coarse grid and then refine details on the fine grid [17]. The resemblance between fine-tuning techniques and multi-scale methods motivates our Multi-Level Fine-Tuning (MLFT) algorithm. Since numerical solvers on coarser grids usually occupy less time due to the scaling laws, we may generate a great more of training samples with a coarse-grid numerical solver. The source task of MLFT is to fit the regression network on training samples generated at the coarse grid, approximating the coarse-grid solver. Because of the large number of coarse-grid samples, we may obtain a good approximation to the coarse-grid solver. From the perspective of multi-scale methods, approximation to the coarse-grid solver provides macroscopic information about the fine-grid solver (and the solution map) which we want to approximate ultimately. However, even if we have a good approximation to the coarse-grid solver, we still need to compensate for the difference between coarse-grid and fine-grid solvers. Therefore, in the target task of MLFT, we fine-tune the regression network on a few training samples generated at the fine grid, approximating the fine-grid solver. The fine-tuning step transfers information from the source task to the target task and hence reduces the generalization error in approximating the fine-grid solver. In words of multi-scale methods, microscopic information gets refined in the fine-tuning step.

In essence, the algorithm of two-level MLFT first trains the regression network on samples generated at the coarse grid, and then fine-tunes the the network on samples generate at the fine grid. The weights and biases learned at the previous level of coarse grid are refined at the level of fine grid. We take the problem of non-linear Schrödinger equation as an example. As mentioned before, we aim to approximate the fine-grid solver with grid step $h_2 = h = 1/320$. We assume that we generate M_2 training samples at the fine grid and each one takes time t_2 . We also introduce a coarse-grid solver with grid step $h_1 = 1/40$ to generate M_1 training samples at the coarse grid, each of which takes time t_1 . We observe from experiment that $t_2 = 64t_1$. The two-level MLFT algorithm consists of two stages: (1) we first initialize a regression network NN and fit it on the M_1 coarse-grid training samples and (2) we then fine-tune the regression network NN to fit the M_2 fine-grid training samples. Given the budget of time $T = 32t_2$ for generating training samples, we have the constraint $M_1t_1 + M_2t_2 = T$ or $M_1/64 + M_2 = 32$. We expect a reduction of generalization error using the two-level MLFT algorithm (e.g., $M_1 = 1024$ coarse-grid samples and $M_2 = 16$ fine-grid samples) compared to directly fitting only on $M_2 = T/t_2 = 32$ fine-grid samples. We also expect the error of MLFT to be lower than the difference between fine-grid and coarse-grid solvers, or equivalently the testing error on fine-grid samples of a regression network trained only with $M_1 = T/t_1 = 2048$ coarse-grid samples. The comparison is shown in [Figure 1](#).

By choosing a sequence of increasingly finer grids with grid step $h_1 > h_2 > \dots > h_L$, the two-level framework can be generalized to L levels: we first train the regression network on samples generated at the coarsest grid (h_1) and then successively fine-tune the network on samples generated at finer grids (h_2 , and then h_3 , and so on till h_L). We assume that M_l training samples are generated by invoking the numerical solver on the grid with grid step h_l and each one takes time t_l on average, where $t_1 < t_2 < \dots < t_L$. If an estimator to the generalization error is available in the form $\hat{g}_L(M_1, M_2, \dots, M_L)$, we may optimize for the smallest estimated generalization error under the constraint of budget of time T for generating training samples:

$$\begin{aligned}
 & \text{minimize} && \hat{g}_L(M_1, M_2, \dots, M_L), \\
 (1.6) \quad & \text{subject to} && M_1t_1 + M_2t_2 + \dots + M_Lt_L = T, \\
 & \text{with respect to} && M_1, M_2, \dots, M_L > 0.
 \end{aligned}$$

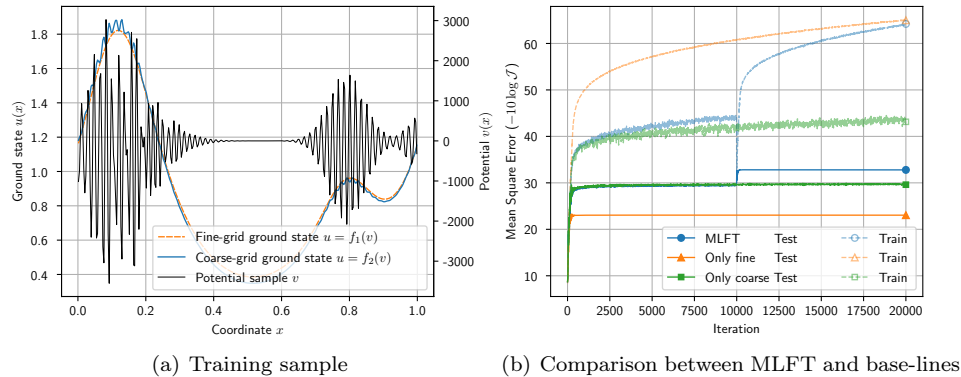


FIG. 1. The non-linear Schrödinger equation problem. Since it is free to choose the finest grid of interest, we choose a fine grid with grid step $h_2 = 1/320$ and turn to approximate the fine-grid numerical solver f_2 with a regression network. For MLFT, we introduce a coarse grid with grid step $h_1 = 1/40$ and a coarse-grid numerical solver f_1 . We plot a training sample generated by the two numerical solvers in (a). In the comparison of loss curves (b), setting “MLFT” trains the regression network on $M_1 = 1024$ coarse-grid samples and then fine-tune on $M_2 = 16$ fine-grid samples, “Only coarse” trains on $M_1 = 2048$ coarse-grid samples, and “Only fine” trains on $M_2 = 32$ fine-grid samples. The networks are tested on fine-grid samples. We observe that the final testing error of MLFT is smaller than using either only coarse-grid or only fine-grid samples.

This budget distribution problem provides practical guidance to generate training samples at coarse and fine grids which invokes the coarse-grid and fine-grid numerical solvers respectively. In other words, it gives insights on distributing the budget for training data over levels, as in the Multi-Level Monte Carlo (MLMC) algorithm [25].

1.2. Related work. Structures of neural networks have inspired extensive study about hierarchical, multi-grid, and multi-level methods in machine learning, especially for convolutional and residual networks [55, 24, 19, 20, 33]. In comparison, we focus on scales of grids on which numerical solvers are invoked and training samples are generated. The main goal of MLFT is to reduce the generalization error in approximating the finest-grid solver (and the solution map).

Haber et al. considered an algebraic multi-grid method through the lens of optimal control [27]. With designed restriction and interpolation procedures, the neural network can be transformed between scales of grids during training. Varying the depths of networks can also be understood by temporally refining the optimal control problem. In contrast, we have coarse-grid and fine-grid training samples, while only a single neural network is used with the architecture unchanged. To match the size of training samples to the input and output shapes of the regression network, we apply spatial restriction and interpolation operators when generating training samples but not during training or fine-tuning the regression network. Besides, the problems we are considering for scientific computing suffer from scaling laws of time when generating training samples on different grids with numerical solvers. On the contrary, classification and segmentation problems in machine learning need manual labeling, the cost of which generally do not depend on the resolution.

Very recently, Lye et al. also noticed the tradeoff between generalization and training data generation, and they developed the Multi-Level Machine Learning Monte Carlo (ML2MC) algorithm [44]. Telescoping as in MLMC [25], they train one regression network to approximate the coarsest-grid solver and multiple networks to ap-

proximate the difference between adjacent fine-grid and coarse-grid solvers. The final model to approximate the finest-grid solver is the sum of all networks. The generalization errors also add together, similar to the variance in MLMC. In comparison, our initial motivation for MLFT follows from few-shot learning techniques. We deploy only one neural network and fine-tune between collections of samples generated at different grids. Since each level of fine-tuning reduces the distance between the current level solver and the intermediate network, generalization errors in previous levels get corrected in later levels. This results in a form of generalization error different from ML2MC. Additionally, [44] mainly considers the map from parameters to scalar observables. In this paper, we tackle the problem of approximating numerical solvers (and the solution map), the input (parameter) and output (solution) of which are functions on grids and lie in high-dimensional spaces.

Another topic related to MLFT is multi-fidelity modeling [52, 51, 50]. The setting of multi-fidelity models applies to ours: a combination of high-fidelity and low-fidelity models are accessible with different tradeoffs between efficiency and accuracy. The high-fidelity and low-fidelity models correspond to fine-grid and coarse-grid solvers respectively. In comparison, MLFT only accesses models (invokes solvers to generate training samples) of different levels subsequently and is more coarse-grained in terms of combining high-fidelity and low-fidelity models. Meanwhile, we better leverage the nature of neural networks as parameterized statistical models which makes fine-tuning possible. Recent progress in deep learning theory also provides us opportunities to find practical estimators to the generalization error.

1.3. Contribution. We summarize our contribution in this paper as follows.

- (1) We identify the problem of reducing generalization error of regression networks in approximation of solution maps when the budget for generating training samples is limited (section 1).
- (2) We design the Multi-Level Fine-Tuning (MLFT) algorithm to reduce generalization error with inspiration from few-shot learning techniques (section 2).
- (3) We perform analysis under the Neural Tangent Kernel (NTK) regime and construct practical estimators to the generalization error, which further provides guidance to distribute the budget for training data over levels (section 3).
- (4) We show the reduction of generalization error with MLFT in experiments and demonstrate optimizing the number of training samples over levels (section 4).

2. Algorithm. We proceed to present our Multi-Level Fine-Tuning (MLFT) algorithm in this section with details. As pointed out in subsection 1.1, the key idea of MLFT is to first train on samples generated at the coarsest grid and then successively fine-tune on samples generated at finer grids. We introduce the definition of levels and the procedure to generate training samples of different levels in subsection 2.1. We then explain the MLFT algorithm in subsection 2.2 together with the performance evaluation procedure of generalization error. We compare MLFT with Multi-Level Machine Learning Monte Carlo (ML2MC) [44] in subsection 2.3.

2.1. Levels and data. We tackle the problem of approximating solution maps in this paper. For simplicity, we consider problems on a d -dimensional ($d = 1, 2, 3$) domain $\Omega = [0, 1]^d$ with a periodic boundary condition. We consider the parametric PDE problem $\mathcal{N}_v u_v = 0$ where the variable parameter v lies in a function space \mathcal{V} . We aim to approximate the non-linear solution map $F : \mathcal{V} \rightarrow \mathcal{U}$ which maps parameter $v \in \mathcal{V}$ to solution $u_v \in \mathcal{U}$, where \mathcal{U} is the function space of solutions. In the example of non-linear Schrödinger equation, the solution map F is the potential-ground state

map and we can set $\mathcal{V} = \mathcal{U} = C(\Omega)$.

To numerically discretize the solution map F , we choose a finest grid of interest $\Omega_L = \{ih_L : 0 \leq i < N_L\}^d$ of N_L^d evenly spaced nodes with grid step $h_L = 1/N_L$. Since we are considering regular grids, we identify functions on the grid as multi-dimensional arrays in $\mathbb{R}^{N_L^d}$. By discretizing the PDE $\mathcal{N}_v u_v = 0$ on grid Ω_L , we discretize the solution map F to be the finest-grid solver F_L . Since it is free to choose the finest grid step h_L according to practical considerations, the core task is to approximate the finest-grid solver F_L (discretized) instead of the solution map F (continuous). With parameters and solutions discretized as functions on grid Ω_L , we assume the spaces of discretized parameters and solutions to be $\mathcal{V}_L, \mathcal{U}_L \subseteq \mathbb{R}^{N_L^d}$ respectively. In this way, the finest-grid numerical solver on grid Ω_L is $F_L : \mathcal{V}_L \rightarrow \mathcal{U}_L$ which maps discretized parameters (functions on grid Ω_L) to discretized solutions (functions on grid Ω_L), as a discretization to the solution map $F : \mathcal{V} \rightarrow \mathcal{U}$. For example, in the one-dimensional non-linear Schrödinger equation problem, we consider the finest-grid solver on the finest grid with grid step $h_2 = 1/320$. We may directly take the spaces of discretized potentials and ground states to be $\mathcal{V}_2 = \mathcal{U}_2 = \mathbb{R}^{320}$, and the corresponding gradient flow ground state solver [9] is represented as $F_2 : \mathcal{V}_2 \rightarrow \mathcal{U}_2$.

As explained in [subsection 1.1](#), the limited budget for generating training samples results in large generalization error. To reduce the generalization error, MLFT introduces a series of coarser grids. The regression network is fit on training samples generated at the coarser grids before finally fine-tuning on samples generated at the finest grid Ω_L . Formally, we choose a sequence of L increasingly finer grid steps $h_1 > h_2 > \dots > h_{L-1} > h_L$. We apply similar numerical discretization to the parametric PDE $\mathcal{N}_v u_v = 0$ on the grid $\Omega_l = \{ih_l : 0 \leq i < N_l\}^d$ with $N_l = 1/h_l$ for $1 \leq l \leq L-1$ as in the case of the finest grid Ω_L . We assume the spaces of potentials and ground states on grid Ω_l to be $\mathcal{V}_l, \mathcal{U}_l \subseteq \mathbb{R}^{N_l^d}$ respectively, and the numerical solver working on grid Ω_l to be $F_l : \mathcal{V}_l \rightarrow \mathcal{U}_l$. For the example of non-linear Schrödinger equation, we use $L = 2$ levels and introduce a coarse grid with grid step $h_1 = 1/40$ for MLFT. In this case, we set $\mathcal{V}_1 = \mathcal{U}_1 = \mathbb{R}^{40}$ and the coarse-grid solver is represented as $F_1 : \mathcal{V}_1 \rightarrow \mathcal{U}_1$.

To approximate the finest-grid solver F_L , we introduce a regression network NN. By identifying multi-dimensional arrays as functions on grids, the network input and output functions on some grid. In order to capture details on the finest grid of interest Ω_L , we design the network to input and output functions on the finest grid Ω_L , as denoted by $\text{NN} : \mathcal{V}_L \rightarrow \mathcal{U}_L$. In other words, the network NN works on grid Ω_L . In the example of non-linear Schrödinger equation, we adopt a MNN- \mathcal{H} network [20] to approximate the finest-grid solver $F_2 : \mathcal{V}_2 = \mathbb{R}^{320} \rightarrow \mathcal{U}_2 = \mathbb{R}^{320}$. The input and output dimensions of the network are both `[batch_size, 320]`, since the finest grid of interest Ω_2 has $N_2 = 320$ nodes.

However, for $1 \leq l \leq L-1$, the coarse-grid solver F_l works on the coarse grid Ω_l and is not compatible with the input and output dimensions of the network. To generate coarse-grid training samples as functions on grid Ω_L , we introduce restriction operators $R_{L \rightarrow l} : \mathcal{V}_L \rightarrow \mathcal{V}_l$ and interpolation operators $I_{l \rightarrow L} : \mathcal{U}_l \rightarrow \mathcal{U}_L$. We transform the coarse-grid solver $F_l : \mathcal{V}_l \rightarrow \mathcal{U}_l$ to

$$(2.1) \quad f_l = I_{l \rightarrow L} \circ F_l \circ R_{L \rightarrow l} : \mathcal{V}_L \rightarrow \mathcal{U}_L$$

which works on the finest grid Ω_L . We train the network with collections of training samples which are all functions on the finest grid Ω_L but are generated by different level- l solvers f_l . For the non-linear Schrödinger equation problem, the coarse-grid

solver $F_1 : \mathcal{V}_1 = \mathbb{R}^{40} \rightarrow \mathcal{U}_1 = \mathbb{R}^{40}$ generates potential-ground state pairs with spatial resolution $N_1 = 40$, incompatible with the spatial resolution of network $N_2 = 320$. Hence, we introduce a Fourier restriction operator $R_{2 \rightarrow 1} : \mathcal{V}_2 = \mathbb{R}^{320} \rightarrow \mathcal{V}_1 = \mathbb{R}^{40}$ and a bicubic interpolation operator $I_{1 \rightarrow 2} : \mathcal{U}_1 = \mathbb{R}^{40} \rightarrow \mathcal{U}_2 = \mathbb{R}^{320}$. The transformed function of coarse-grid solver is $f_1 = I_{1 \rightarrow 2} \circ F_1 \circ R_{2 \rightarrow 1} : \mathcal{V}_2 = \mathbb{R}^{320} \rightarrow \mathcal{U}_2 = \mathbb{R}^{320}$. We use f_1 instead of F_1 to generate coarse-grid samples for training. For notation convenience, we denote $f_L = F_L$, $R_{L \rightarrow L} = \text{id}_{\mathcal{V}_L}$, and $I_{L \rightarrow L} = \text{id}_{\mathcal{U}_L}$.

We describe the procedure to generate samples at different levels. According to the parameters of interest, we choose a probability distribution \mathcal{D} on \mathcal{V}_L to sample discretized parameters. At level l where $1 \leq l \leq L$, we independently draw M_l parameter samples $\{v_m^l\}_{m=1}^{M_l}$ from \mathcal{D} on grid Ω_L . We then restrict the parameters to grid Ω_l , invoke the coarse-grid solver F_l for solutions on grid Ω_l , and interpolate the solutions to grid Ω_L . Equivalently, we compute $u_m^l = f_l(v_m^l) = I_{l \rightarrow L} \circ F_l \circ R_{L \rightarrow l}(v_m^l)$, as depicted in Figure 2. For finding the optimized number of training samples over levels, we denote the average time to generate a sample at level l by evaluating f_l to be t_l .

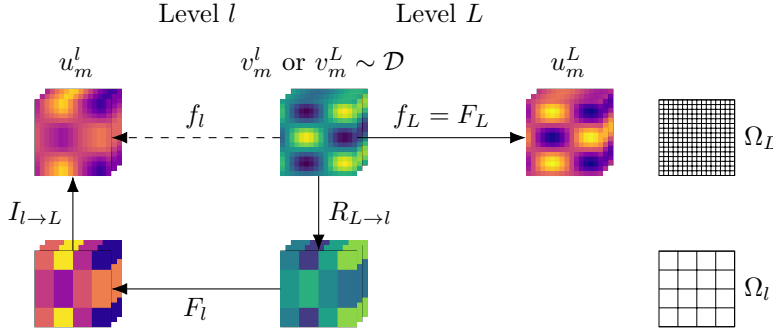


FIG. 2. Schematic illustration on generating samples at levels l and L where $1 \leq l \leq L-1$. For level l , we draw parameter samples from \mathcal{D} on grid Ω_L , restrict the parameters to grid Ω_l , invoke the coarse-grid solver F_l for solutions on grid Ω_l , and interpolate the solutions to grid Ω_L .

2.2. Multi-Level Fine-Tuning algorithm. We describe our Multi-Level Fine-Tuning (MLFT) algorithm. In order to approximate the solution map $F : \mathcal{V} \rightarrow \mathcal{U}$, we deploy a regression neural network $\text{NN} : \mathcal{V}_L \rightarrow \mathcal{U}_L$ to approximate the finest-grid numerical solver $f_L : \mathcal{V}_L \rightarrow \mathcal{U}_L$. With only one level $l = L$, we fit the neural network on training samples generated at level l as described in subsection 2.1. We use the Mean Square Error (MSE), or equivalently the squared L^2 norm on grid Ω_L for this training (fitting) process as in Algorithm 2.1. We introduce the schematic illustration in the function space $\mathcal{V}_L \rightarrow \mathcal{U}_L$ in Figure 3.

The single-level training of a regression network at level $l = L$ is the most direct approach to approximate the finest-grid solver f_L . Single-level training at level $l = L$ serves as a base-line for comparison. As mentioned in subsection 1.1, since neural networks usually fit exactly at the training samples, the generalization error in approximating the finest-grid solver f_L is of major concern. Hence, we evaluate the generalization error g_L in approximating the finest-grid solver f_L for performance comparison:

$$(2.3) \quad g_L = g_L^{\text{test}} - g_L^{\text{train}}, \quad \begin{cases} g_L^{\text{test}} = \mathbb{E}_{v \sim \mathcal{D}} \|f_L(v) - \text{NN}(v)\|_2, \\ g_L^{\text{train}} = \sum_{m=1}^{M_L} \|u_m^L - \text{NN}(v_m^L)\|_2 / M_L. \end{cases}$$

Algorithm 2.1 Train a regression network at a single level l

Generate M_l training samples $\{(v_m^l, u_m^l)\}_{m=1}^{M_l}$ with $u_m^l = f_l(v_m^l)$ at level l
 Initialize a neural network NN which works on grid Ω_L
 Fit NN on $\{(v_m^l, u_m^l)\}_{m=1}^{M_l}$ by minimizing the Mean Square Error (MSE)

$$(2.2) \quad \mathcal{J}_l = \frac{1}{M_l} \sum_{m=1}^{M_l} \|u_m^l - \text{NN}(v_m^l)\|_{L^2}^2$$

return Trained regression neural network NN

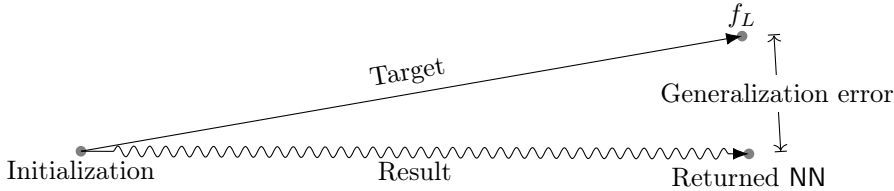


FIG. 3. Schematic illustration of [Algorithm 2.1](#) (single-level training at level $l = L$) in the function space. In this illustration, points represent functions in $\mathcal{V}_L \rightarrow \mathcal{U}_L$: we aim to approximate the finest-grid solver f_L (a function from \mathcal{V}_L to \mathcal{U}_L) by a regression network NN (a parameterized function from \mathcal{V}_L to \mathcal{U}_L). We target to compensate for the difference between the initialized network and the finest-grid solver f_L (“Target”), and during training the network moves in the function space (“Result”). When the training error g_L^{train} vanishes, difference between the trained regression network NN and the finest-grid solver f_L is the generalization error $g_L = g_L^{\text{test}}$.

Here we use the vector 2-norm (instead of L^2 -norm on grid Ω_L) in consistence with the notation in [section 3](#). We expect $g_L^{\text{train}} \ll g_L^{\text{test}}$ and $g_L \approx g_L^{\text{test}}$. Another base-line for comparison is the single-level training only with samples generated at a coarse grid, for example, the single-level training at level $l = L - 1$. In this case, we evaluate the testing error for performance comparison since we do not train at level L :

$$(2.4) \quad g_L = g_L^{\text{test}} = \mathbb{E}_{v \sim \mathcal{D}} \|f_L(v) - \text{NN}(v)\|_2.$$

The regression network approximates the coarse-grid solver f_{L-1} instead of the finest-grid solver f_L , so we expect $g_L \gtrsim e_L$ where e_L is the difference in between:

$$(2.5) \quad e_L = \mathbb{E}_{v \sim \mathcal{D}} \|f_L(v) - f_{L-1}(v)\|_2.$$

As mentioned in [subsection 1.1](#), our MLFT algorithm first trains the regression neural network on samples generated at the coarsest grid and then successively fine-tunes the network on samples generated at finer grids. The MLFT algorithm is described in [Algorithm 2.2](#) together with the function space illustration in [Figure 4](#). Similar to the single-level training, MSE (2.2) is used as the loss function for the regression network to fit the training samples. Since we deploy only one neural network NN, there is only one initialization step. In the following fine-tuning steps, we do not freeze parameters (weights and biases) of the neural network, nor modify the network architecture. We have not observed apparent over-fitting phenomenon in numerical experiments approximating solution maps and numerical solvers (e.g., [Figures 1, 11](#) and [14](#)), so we do not apply extra regularization either. The optimizer is not restart but we keep the momentum vector (for Momentum [\[53\]](#)) or the estimation of moments (for Adam [\[38\]](#)). For simplicity, parameters of the optimizer like step sizes are retained during the whole training and fine-tuning process.

Algorithm 2.2 Multi-Level Fine-Tune (MLFT) a regression network

Generate M_1 samples $\{(v_m^1, u_m^1)\}_{m=1}^{M_1}$ with $u_m^1 = f_1(v_m^1)$
Initialize a neural network NN which works on grid Ω_L
Fit NN on $\{(v_m^1, u_m^1)\}_{m=1}^{M_1}$ by minimizing MSE
{Train NN from initialization to f_1 }

for $l = 2$ **to** L **do**
Generate M_l samples $\{(v_m^l, u_m^l)\}_{m=1}^{M_l}$ with $u_m^l = f_l(v_m^l)$
Fit NN on $\{(v_m^l, u_m^l)\}_{m=1}^{M_l}$ by minimizing MSE
{Fine-tune NN to f_l }

end for
return Trained and fine-tuned regression neural network NN

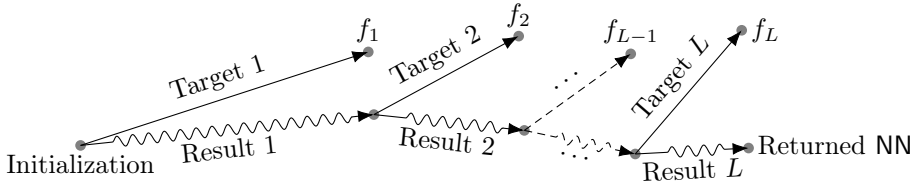


FIG. 4. Schematic illustration of [Algorithm 2.2](#) (MLFT) in the function space. We mark the training targets (“Target l ”) and the obtained results (“Result l ”) at level l , as in [Figure 3](#).

2.3. Multi-Level Machine Learning Monte Carlo algorithm. In [\[44\]](#), Lye et al. proposed a multi-level algorithm for regression networks named Multi-Level Machine Learning Monte Carlo (ML2MC) with inspiration from Multi-Level Monte Carlo (MLMC) [\[25\]](#). In the paper [\[44\]](#), the problem of approximating parameter-observable maps of parametric PDEs is considered, where the observables are scalars. We make slight modifications to match our setting of approximating solution maps (parameter-solution maps), whose inputs and outputs are functions on grids.

The algorithm of ML2MC constructs a telescoping series as in MLMC

$$(2.6) \quad f_L = f_1 + (f_2 - f_1) + (f_3 - f_2) + \cdots + (f_L - f_{L-1}).$$

One regression network is used to approximate f_1 and other $L - 1$ networks to approximate $f_l - f_{l-1}$ for $2 \leq l \leq L$ respectively. For an approximation to the finest-grid solver f_L , one sums the L separately-trained networks together, as explained in [Algorithm 2.3](#) and [Figure 5](#).

The main difference between MLFT ([Algorithm 2.2](#)) and ML2MC ([Algorithm 2.3](#)) is two-fold. The first difference is that we fine-tune one regression network instead of summing several separately-trained networks. We make use of the difference between parameterized model fitting and Monte Carlo estimation: fine-tuning may correct generalization errors accumulated in previous levels, while variances of multiple independent estimators (and generalization errors of several separately-trained networks) add together. As a result, the form of generalization error of MLFT is different from that of ML2MC, as will be analyzed in [section 3](#). Another difference lies in the usage of neural networks. In MLFT, we are able to confine all the computation into a single neural network thanks to the fine-tuning technique. This saves graphic memory and avoids restarting the optimizer: modern first-order optimizers memorize historical information for acceleration [\[53, 38\]](#). Moreover, insights from curriculum learning [\[61\]](#) tell that we may gain much more. If a parameterized statistical model is trained on

Algorithm 2.3 Multi-Level Machine Learning Monte Carlo (ML2MC) for regression networks [44]

Generate M_1 samples $\{(v_m^1, u_m^1)\}_{m=1}^{M_1}$ with $u_m^1 = f_1(v_m^1)$
Initialize a neural network NN_1 which works on grid Ω_L
Fit NN_1 on $\{(v_m^1, u_m^1)\}_{m=1}^{M_1}$ by minimizing MSE
{Fit NN_1 from initialization to f_1 }

for $l = 2$ **to** L **do**
Generate M_l samples $\{(v_m^l, u_m^l)\}_{m=1}^{M_l}$ with $u_m^l = f_l(v_m^l) - f_{l-1}(v_m^l)$
Initialize a neural network NN_l which works on grid Ω_L
Fit NN_l on $\{(v_m^l, u_m^l)\}_{m=1}^{M_l}$ by minimizing MSE
{Fit NN_l from initialization to $f_l - f_{l-1}$ }

end for
return Sum of trained regression neural networks $\sum_{l=1}^L \text{NN}_l$

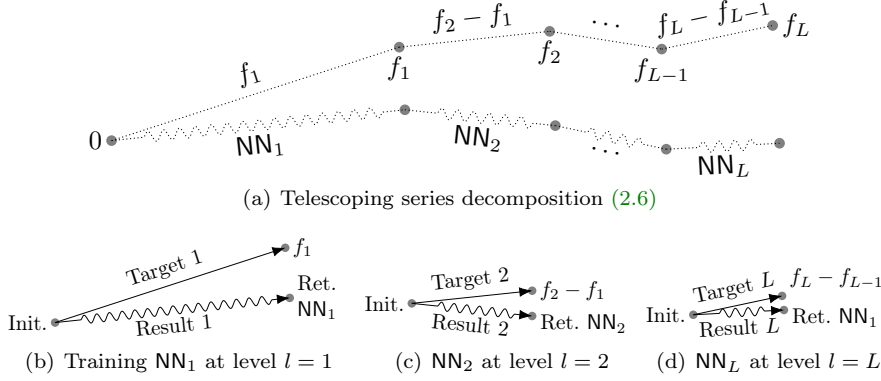


FIG. 5. Schematic illustrations of *Algorithm 2.3* (ML2MC) in the function space. Function of the finest-grid solver f_L is decomposed by the telescoping series (2.6) as shown in (a), and then L neural networks NN_l are trained separately at level l for $1 \leq l \leq L$, as shown in (b), (c), and (d).

easy tasks before moving on to more difficult ones, the training process on difficult tasks can get boosted significantly. In our setting, approximating the finest-grid solver f_L which contains more details can be more difficult than approximating coarse-grid solvers f_l where $1 \leq l \leq L - 1$. In correspondence, we observe faster convergence in the fine-tuning steps of MLFT compared to ML2MC, as shown in experiments of [section 4](#) and [Figure 11](#).

3. Analysis. We analyze our algorithm of MLFT under assumptions in this section. In the MLFT algorithm, at level l , we fit the regression network on training samples $\{(v_m^l, u_m^l)\}_{m=1}^{M_l}$ where $u_m^l = f_l(v_m^l)$ to approximate the solver f_l where $1 \leq l \leq L$. As a result, generalization errors are presented at the training or fine-tuning process at each level. We consider bounds of the generalization error at each level citing results of Neural Tangent Kernel (NTK) and Rademacher complexity of kernel classes in [subsections 3.1](#) and [3.2](#). We then chain the generalization errors at each level under guidance of empirical observations and construct *a priori* error estimator \hat{g}_L to the generalization error g_L of MLFT in approximating the finest-grid solver in [subsection 3.3](#). We try to get rid of pessimistic estimations and extend to finite-width cases not solidly covered by the infinite-width NTK theory by introducing practical

a *posteriori* error estimator \hat{g}_L by fitting coefficients into the form of generalization error in [subsection 3.4](#).

In this section, we consider the training process in the function space $\mathcal{V}_L \rightarrow \mathcal{U}_L$ as in [\[32\]](#) and [Figures 3 to 5](#). We denote the function of NN at initialization as \hat{f}_0 , together with \hat{f}_l for the intermediate model right after training or fine-tuning at level l . In terms of functions, the level l involves training or fine-tuning the regression network which is initially \hat{f}_{l-1} to fit the target f_l on training samples (“Target l ” in [Figure 4](#)), and the network eventually moves from \hat{f}_{l-1} to \hat{f}_l (“Result l ” in [Figure 4](#)). We denote the generalization error of training or fine-tuning at level l to be

$$(3.1) \quad g_l = g_l^{\text{test}} - g_l^{\text{train}} = \mathbb{E}_{v \sim \mathcal{D}} \|f_l(v) - \hat{f}_l(v)\|_2 - \frac{1}{M_l} \sum_{m=1}^{M_l} \|u_m^l - \hat{f}_l(v_m^l)\|_2.$$

The key observation in introducing the function space illustrations is that in the Neural Tangent Kernel (NTK) regime, fitting the regression neural network on training samples converges to kernel “ridgeless” regression [\[42\]](#). The kernel “ridgeless” regression is linear with respect to the dependent variable (usually referred to as y in contrast to independent variables x). In our case, it turns out that at level l the increment $\hat{f}_l - \hat{f}_{l-1}$ (“Result l ” in [Figure 4](#)) and the error $f_l - \hat{f}_l$ in the function space only depend on the initial difference $f_l - \hat{f}_{l-1}$ (“Target l ” in [Figure 4](#)) but not the starting point \hat{f}_{l-1} . This is critical to our construction of estimators to the generalization error. We briefly introduce the idea in [Figure 6](#).

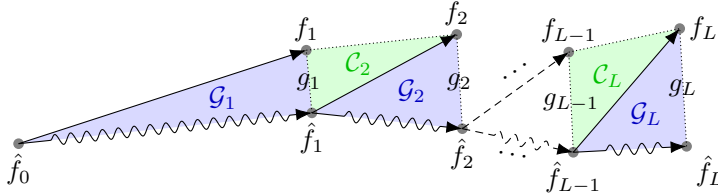


FIG. 6. Schematic illustration of notations and the construction of error estimators (cf. [Figure 4](#)). For triangles \mathcal{G}_l , we estimate the Generalization error g_l (i.e., $f_l - \hat{f}_l$) from the initial difference at training samples $u_m^l - \hat{f}_{l-1}(v_m^l)$ (i.e., $f_l - \hat{f}_{l-1}$). For triangles \mathcal{C}_l , we Combine the generalization error g_{l-1} (i.e., $f_{l-1} - \hat{f}_{l-1}$) and the difference of training samples between levels $u_m^l - \hat{f}_{l-1}(v_m^l)$ (i.e., $f_l - \hat{f}_{l-1}$) to estimate the initial difference at training samples $u_m^l - \hat{f}_{l-1}(v_m^l)$ (i.e., $f_l - \hat{f}_{l-1}$). By chaining the triangles, we obtain an error estimator to the generalization error g_L in approximating the finest-grid solver f_L .

3.1. Neural Tangent Kernel. To understand the optimization and generalization of neural networks, one particular approach is to consider the infinite-width limit of neural networks in the function space [\[32, 40\]](#). Under the Neural Tangent Kernel (NTK) parameterization and random unit Gaussian initialization, channels of a neural network behave like independent samples. Hence, the law of large numbers can be cited, proving the convergence of the neural network to a Gaussian process.

Formally speaking, we denote the output of the network to be $\text{NN}(v) = f(v; \theta) \in \mathbb{R}^{N^d}$ with input v and parameter (weights and biases) θ . We consider NTK parameterization for NN, which scales the output of each layer by $1/\sqrt{C}$ where C is the number of channels in the layer [\[32\]](#). By recognizing the output $f(v; \theta)$ as a column vector, the Conjugate Kernel (CK, also known as Neural Network Gaussian Process

or NNGP) is defined as

$$(3.2) \quad \Sigma(v, v') = \mathbb{E}_\theta f(v; \theta) f^\top(v'; \theta) \in \mathbb{R}^{N_L^d \times N_L^d},$$

where the expectation is taken with respect to random unit Gaussian initialization of θ . When the numbers of channels C go to infinity, Σ converges and the function $v \mapsto f(v; \theta)$ (random because of random initialization of θ) turns out to be the centered matrix-valued Gaussian process with covariance kernel Σ [32].

Similarly, the Neural Tangent Kernel (NTK) is defined as

$$(3.3) \quad \Theta(v, v') = \sum_{\theta} \frac{df(v; \theta)}{d\theta} \frac{df^\top(v'; \theta)}{d\theta} \in \mathbb{R}^{N_L^d \times N_L^d},$$

where the sum is taken over all entries of the parameter θ . As pointed out by [32], Θ converges almost surely at random unit Gaussian initialization of θ in the infinite-width limit. In the case of gradient descent, NTK stays asymptotically constant during training [32]. A closed-form formula of the converged CK Σ and NTK Θ is available for various neural network architectures (including dense layers, convolutional layers, and ReLU activation layers) [5]. Software package has been developed to compute CK Σ and NTK Θ both in the infinite-width limit and for a finite-width network [48].

We summarize our assumptions for the following analysis. We assume NTK parameterization and random unit Gaussian initialization of the neural network. Moreover, we assume the network is infinitely wide so that we consider the NTK regime. The influence of finite width is discussed in [subsection SM4.2](#). We assume that Θ is a symmetric positive definite kernel, which can be proved under assumptions (e.g., when norms of inputs are bounded both above and below, i.e., $\Theta(1)$) [32, 15]. In this case, Θ itself induces a Reproducing Kernel Hilbert Space (RKHS), which we denote by \mathcal{H} . According to [14], because of the architecture of neural networks, we have $\Sigma \prec \Theta$ and hence $\hat{f}_0 \in \mathcal{H}$. Additionally, we assume that the target at each level, namely the function of numerical solver satisfy $f_l \in \mathcal{H}$. This means that the functions f_l are learnable under kernel “ridgeless” regression with NTK Θ . The learnability of certain functions with NTK has been proved [4].

At level l , we train a regression network to fit M_l training samples $\{(v_m^l, u_m^l)\}_{m=1}^{M_l}$ by minimizing MSE (equivalent to (2.2) up to a constant)

$$(3.4) \quad \mathcal{J}_l[f] = \frac{1}{M_l} \sum_{m=1}^{M_l} \|u_m^l - f(v_m^l; \theta)\|_2^2.$$

According to the framework of NTK [32], the gradient descent dynamics on (3.4) of an infinitely wide network in the function space \mathcal{H} turns out to be a linear ordinary differential equation

$$(3.5) \quad \frac{df(v)}{dt} = \sum_{\theta} \frac{df(v; \theta)}{d\theta} \frac{d\theta}{dt} = \frac{1}{M_l} \sum_{m=1}^{M_l} \Theta(v, v_m^l) (u_m^l - f(v_m^l)).$$

Since the training or fine-tuning process at level l fits the regression network to training samples generated by the level- l solver f_l , we have $u_m^l = f_l(v_m^l)$ and $f|_{t=0} = \hat{f}_{l-1}$. By introducing the Gram operator $\Pi \in \mathcal{L}(\mathcal{H})$, (3.5) turns out to be

$$(3.6) \quad \frac{df}{dt} = \Pi(f_l - f), \quad \Pi[f](v) = \frac{1}{M_l} \sum_{m=1}^{M_l} \Theta(v, v_m^l) f(v_m^l).$$

Since the Gram operator Π is self-adjoint, positive semi-definite, and finite-rank in \mathcal{H} , solution f of (3.6) converges when $t \rightarrow +\infty$. We assume that we train the regression network for sufficiently long time at level l . In this case, the infinite-time limit $f|_{t \rightarrow +\infty} = \hat{f}_l$. Moreover, due to the assumption that NTK Θ is symmetric positive definite, the neural network indeed fits exactly at the training samples $\{(v_m^l, u_m^l)\}_{m=1}^{M_l}$. This can be summarized as the following theorem [32]. Specifically, the increment $\hat{f}_l - \hat{f}_{l-1}$ at level l (“Result l ” in Figure 4) only depends on the initial difference $f_l - \hat{f}_{l-1}$ (“Target l ” in Figure 4) but not the specific function \hat{f}_{l-1} . Thanks to this observation, we are able to construct error estimators to the generalization error as in Figure 6 and subsection 3.3.

THEOREM 3.1. *Assume the NTK Θ to be symmetric positive definite and $\hat{f}_0, f_l \in \mathcal{H}$ for $1 \leq l \leq L$. Let \mathcal{M}_l be the space spanned by column spaces of $\Theta(\cdot, x_m^l)$ for $1 \leq m \leq M_l$ and $P_{\mathcal{M}_l}$ be the orthogonal projection operator onto \mathcal{M}_l in \mathcal{H} . Then, for $1 \leq l \leq L$, it holds that*

$$(3.7) \quad \hat{f}_l - \hat{f}_{l-1} = P_{\mathcal{M}_l} \left(f_l - \hat{f}_{l-1} \right).$$

Specifically, $\hat{f}_l \in \mathcal{H}$ for $1 \leq l \leq L$, and $\hat{f}_l(v_m^l) = f_l(v_m^l) = u_m^l$ for $1 \leq m \leq M_l$.

3.2. Generalization in the Neural Tangent Kernel regime. We then consider the generalization error of regression network in the NTK regime (infinite-width limit). Generalization errors of neural networks have been extensively studied from the perspective of kernel methods [11, 4, 14]. Owing to the introduction of NTK, fitting a neural network is equivalent to performing kernel “ridgeless” regression with NTK Θ . As a result, the generalization error g_l in approximating the level- l solver function f_l is related to the Rademacher complexity of kernel classes with NTK Θ .

3.2.1. Kernel “ridgeless” regression. We have studied the increment $\hat{f}_l - \hat{f}_{l-1}$ at level l in the function space in Theorem 3.1. However, what we are really interested is the RKHS norm $\|\hat{f}_l - \hat{f}_{l-1}\|_{\mathcal{H}}$, which controls the size of hypothesis space and determines the Rademacher complexity. The RKHS norm can be derived from the fact that fitting a neural network is equivalent to performing kernel “ridgeless” regression with NTK Θ [32]. (For a detailed exposition on kernel methods, see [29, 46].)

The kernel “ridgeless” regression is the limit of kernel ridge regression with diminishing ridge regularization. The kernel “ridgeless” regression has been recently found to generalize [11, 42]. In our setting, the result function $\hat{f}_l = \hat{f}_{l-1} + P_{\mathcal{M}_l}(f_l - \hat{f}_{l-1})$ is exactly the solution \hat{f}^* to the optimization problem of kernel “ridgeless” regression:

$$(3.8) \quad \begin{aligned} & \text{minimize} && \|\hat{f} - \hat{f}_{l-1}\|_{\mathcal{H}}, \\ & \text{subject to} && \hat{f}(v_m^l) = f_l(v_m^l) = u_m^l, \quad 1 \leq m \leq M_l, \\ & && \text{with respect to } \hat{f} \in \mathcal{H}. \end{aligned}$$

Denote the $\mathbf{G}_l \in \mathbb{R}^{M_l N_L^d \times M_l N_L^d}$ to be the Gram matrix and $\mathbf{f}_l(\mathbf{v}^l) \in \mathbb{R}^{M_l N_L^d}$ (and also $\hat{\mathbf{f}}_l(\mathbf{v}^l)$) to be vectorized functions on training samples v_m^l :

$$(3.9) \quad \mathbf{G}_l := \begin{bmatrix} \Theta(v_1^l, v_1^l) & \Theta(v_1^l, v_2^l) & \cdots & \Theta(v_1^l, v_{M_l}^l) \\ \Theta(v_2^l, v_1^l) & \Theta(v_2^l, v_2^l) & \cdots & \Theta(v_2^l, v_{M_l}^l) \\ \vdots & \vdots & \ddots & \vdots \\ \Theta(v_{M_l}^l, v_1^l) & \Theta(v_{M_l}^l, v_2^l) & \cdots & \Theta(v_{M_l}^l, v_{M_l}^l) \end{bmatrix}, \quad \mathbf{f}_l(\mathbf{v}^l) := \begin{bmatrix} f_l(v_1^l) \\ f_l(v_2^l) \\ \vdots \\ f_l(v_{M_l}^l) \end{bmatrix}.$$

Using the kernel trick, the solution $\hat{f}_l = \hat{f}^*$ to (3.8) can be written as (cf. (3.7)) [29]

$$(3.10) \quad \hat{f}_l = \hat{f}_{l-1} + \sum_{m=1}^{M_l} \Theta(\cdot, v_m^l) \alpha_m, \quad \alpha = \mathbf{G}_l^{-1}(\mathbf{f}_l(\mathbf{v}^l) - \hat{\mathbf{f}}_{l-1}(\mathbf{v}^l)),$$

where $\alpha_m \in \mathbb{R}^{N_L^d}$ are column vectors and α is their vectorization as in (3.9). Abbreviating $\langle \mathbf{u}, \mathbf{w} \rangle_{\mathbf{G}_l^{-1}} = \mathbf{w}^\top \mathbf{G}_l^{-1} \mathbf{u}$ and $\|\mathbf{u}\|_{\mathbf{G}_l^{-1}} = \sqrt{\langle \mathbf{u}, \mathbf{u} \rangle_{\mathbf{G}_l^{-1}}}$, the RKHS norm is

$$(3.11) \quad \|\hat{f}_l - \hat{f}_{l-1}\|_{\mathcal{H}} = \|\alpha\|_{\mathbf{G}_l} = \|\mathbf{f}_l(\mathbf{v}^l) - \hat{\mathbf{f}}_{l-1}(\mathbf{v}^l)\|_{\mathbf{G}_l^{-1}}.$$

This result is summarized as the following theorem [29].

THEOREM 3.2. *Assume the NTK Θ to be symmetric positive definite and $\hat{f}_0, f_l \in \mathcal{H}$ for $1 \leq l \leq L$. Then, for $1 \leq l \leq L$,*

$$(3.12) \quad \|\hat{f}_l - \hat{f}_{l-1}\|_{\mathcal{H}} = \|\mathbf{f}_l(\mathbf{v}^l) - \hat{\mathbf{f}}_{l-1}(\mathbf{v}^l)\|_{\mathbf{G}_l^{-1}}.$$

3.2.2. Rademacher complexity of kernel classes. The complexity of hypothesis space of kernel classes can be delineated by Rademacher complexity [46]. With the RKHS norm $\|\hat{f}_l - \hat{f}_{l-1}\|_{\mathcal{H}}$ given in Theorem 3.2, we are going to consider the Rademacher complexity of \mathcal{H} -balls centered at $\hat{f}_{l-1} \in \mathcal{H}$.

$$(3.13) \quad \mathcal{B}(\hat{f}_{l-1}, D) = \{f \in \mathcal{H} : \|f - \hat{f}_{l-1}\|_{\mathcal{H}} \leq D\}.$$

We follow [45, 57] to define the Rademacher complexity of vector-valued functions (in \mathcal{H}) and matrix-valued kernels (NTK Θ). Given samples $\{v_m^l\}_{m=1}^{M_l} \subseteq \mathcal{V}_L$ and random testing vectors $\{\nu_m\}_{m=1}^{M_l}$ in $\mathbb{R}^{N_L^d}$, we define the empirical Rademacher complexity of a vector-valued function class \mathcal{F} from \mathcal{V}_L to $\mathbb{R}^{N_L^d}$ to be

$$(3.14) \quad \hat{\mathfrak{R}}_{v^l, \nu}(\mathcal{F}) := \frac{1}{M_l} \mathbb{E}_{\sigma, \nu} \sup_{f \in \mathcal{F}} \sum_{m=1}^{M_l} \sigma_m \nu_m^\top f(v_m^l)$$

Here σ_m are independent Bernoulli-like random variables which take the value ± 1 with equal probability. As a variant of the Rademacher complexity of scalar-valued kernel classes [10, 46], we have the following theorem. Detailed proof is given in section SM1.

THEOREM 3.3. *Assume $\|\Theta(v_m^l, v_m^l)\|_2 \leq R^2$ for $1 \leq m \leq M_l$. If the normalization condition $\|\nu_m\|_2 \equiv 1$ and the independence condition $\nu_m \perp \sigma_m$ are satisfied for $1 \leq m \leq M_l$, then it holds that*

$$(3.15) \quad \hat{\mathfrak{R}}_{v^l, \nu}(\mathcal{B}(\hat{f}_{l-1}, D)) \leq \frac{DR}{\sqrt{M}}.$$

We then consider the Rademacher complexity of loss classes, for adaptation to Theorem 1.1. Since we aim to approximate the level- l solver function f_l as ground-truth at level l , we define the loss class of $\mathcal{B}(\hat{f}_{l-1}, D)$ to be

$$(3.16) \quad \mathcal{L}(\hat{f}_{l-1}, D; f_l, B_l) = \{v \mapsto \|f_l(v) - f(v)\|_2 \wedge B_l : f \in \mathcal{B}(\hat{f}_{l-1}, D)\}.$$

Here B_l is a cutoff constant to bound the loss function. We imitate [46] to derive the Rademacher complexity of loss classes of vector-valued functions in the following theorem. The proof can be found in section SM1.

THEOREM 3.4. *Assume $\|\Theta(v_m^l, v_m^l)\|_2 \leq R^2$ for $1 \leq m \leq M_l$. Then, it holds that*

$$(3.17) \quad \hat{\mathfrak{R}}_{v^l}(\mathcal{L}(\hat{f}_{l-1}, D; f_l, B_l)) \leq \frac{DR}{\sqrt{M}}.$$

3.2.3. Generalization of kernel classes. We finally consider bounds of the generalization error in approximating the level- l solver function using NTK kernel classes. As an application of [Theorems 1.1 and 3.4](#) and a variant of [\[4\]](#), we have the following theorem which is proved in [section SM1](#). Since the network fits exactly at the training samples as in [Theorem 3.1](#), the term of training error is absent in [\(3.18\)](#).

THEOREM 3.5. *Assume $\|\Theta(v, v)\|_2 \leq R^2$ for all v in the support of \mathcal{D} . Then, with probability $1 - \delta$ on generating training samples $\{(v_m^l, u_m^l)\}_{m=1}^{M_l}$, it holds that*

$$(3.18) \quad \mathbb{E}_{v \sim \mathcal{D}} (\|f_l(v) - \hat{f}_l(v)\|_2 \wedge B_l) \leq \frac{2R \|\mathbf{f}_l(\mathbf{v}^l) - \hat{\mathbf{f}}_{l-1}(\mathbf{v}^l)\|_{\mathbf{G}_l^{-1}}}{\sqrt{M_l}} + \frac{2B_l R}{\sqrt{M_l}} + 3B_l \sqrt{\frac{\log K_l / \delta}{2M_l}},$$

where $K_l = \lceil \|\mathbf{f}_l - \hat{\mathbf{f}}_{l-1}\|_{\mathcal{H}} / B_l \rceil$.

3.3. A priori error estimator. We aim to find estimators to the generalization error g_L in approximating the finest-grid solver f_L . Since under assumptions the network fits exactly at the training samples at level l (cf. [Theorem 3.1](#)), the generalization error [\(3.1\)](#) turns out to be $g_l = \mathbb{E}_{v \sim \mathcal{D}} \|f_l(v) - \hat{f}_l(v)\|_2$. We have already mentioned the equivalence between neural network and kernel “ridgeless” regression with NTK Θ and considered the generalization error of NTK kernel classes in [Theorem 3.5](#). The remaining task is to apply [Theorem 3.5](#) in practical cases and chaining the generalization error as introduced in [Figure 6](#). In this subsection, we aim to find the *a priori* error estimator which can be computed before performing MLFT. We provide empirical observations to justify our construction of the estimator.

3.3.1. Estimating g_1 . As mentioned in [Figure 6](#), we apply [Theorem 3.5](#) in the triangle \mathcal{G}_1 to estimate the generalization error g_1 . For training at level $l = 1$, the main term in the right hand side of [\(3.18\)](#) is the complexity $\hat{\mathfrak{R}}_1 = 2R \|\mathbf{f}_1(\mathbf{v}^1) - \hat{\mathbf{f}}_0(\mathbf{v}^1)\|_{\mathbf{G}_1^{-1}} / \sqrt{M_1}$. In the example of non-linear Schrödinger equation, we try with different M_1 and plot the correlation between complexity $\hat{\mathfrak{R}}_1$ and the generalization error g_1 in [Figure 7 \(a\)](#).

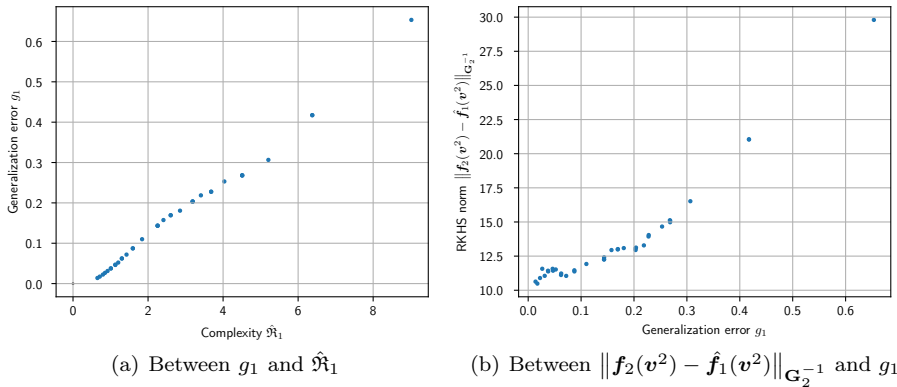


FIG. 7. Correlation between key quantities in the triangle \mathcal{G}_1 and \mathcal{C}_2 of [Figure 6](#). Detailed discussion on the computation is presented in [subsection SM4.3](#).

With the clear linear correlation in [Figure 7 \(a\)](#) as empirical justification, we

consider the *a priori* estimator to g_1 :

$$(3.19) \quad \hat{g}_1 = \frac{2Rc_1}{\sqrt{M_1}}, \quad c_1 = \|\mathbf{f}_1(\mathbf{v}^1) - \hat{\mathbf{f}}_0(\mathbf{v}^1)\|_{\mathbf{G}_1^{-1}}, \quad R = \max_{v \in \text{supp } \mathcal{D}} \sqrt{\|\Theta(v, v)\|_2}$$

For justification of (3.19) from Theorem 3.5, we need to choose an appropriate cutoff B_1 such that (1) $B_1 \gg g_1$, so that we can equate the left hand side of (3.18) with g_1 and (2) $B_1 \ll c_1$, so that the last two terms in (3.18) are negligible. We conclude from Figure 7 (a) that in practice g_1 decreases when M_1 grows (actually in speed $O(1/\sqrt{M_1})$). However, c_1 does not decrease (but actually increases as pointed out in subsection SM4.3), so such B_1 satisfying $g_1 \ll B_1 \ll c_1$ exists for large M_1 . Actually, in the example of non-linear Schrödinger equation, $c_1 = 56.543$ when $M_1 = 16$ (averaged over 64 collections of samples $\{(v_m^1, u_m^1)\}_{m=1}^{M_1}$) and is much greater than g_1 in Figure 7 (a), so such B_1 exists even for a small M_1 . We note that the coefficients c_1 and R can be practically computed without training the regression network.

3.3.2. Estimating $\|\mathbf{f}_l(\mathbf{v}^l) - \hat{\mathbf{f}}_{l-1}(\mathbf{v}^l)\|_{\mathbf{G}_l^{-1}}$ for $2 \leq l \leq L$. As mentioned in Figure 6, in the triangle \mathcal{C}_l , we need to combine the generalization error g_{l-1} at the previous level and the difference between training samples $v_m^l - f_{l-1}(v_m^l) = f_l(v_m^l) - f_{l-1}(v_m^l)$ to estimate the RKHS norm $\|\hat{f}_l - \hat{f}_{l-1}\|_{\mathcal{H}} = \|\mathbf{f}_l(\mathbf{v}^l) - \hat{\mathbf{f}}_{l-1}(\mathbf{v}^l)\|_{\mathbf{G}_l^{-1}}$, which is critical to estimate g_l as in the case of g_1 . In the example of non-linear Schrödinger equation, we plot the RKHS norm $\|\mathbf{f}_2(\mathbf{v}^2) - \hat{\mathbf{f}}_1(\mathbf{v}^2)\|_{\mathbf{G}_2^{-1}}$ at level $l = 2$ with different g_1 in Figure 7 (b) by varying the number of training samples M_1 at level $l = 1$.

We can notice a linear correlation with positive intercept in Figure 7 (b). Only when g_{l-1} is large does $\|\mathbf{f}_l(\mathbf{v}^l) - \hat{\mathbf{f}}_{l-1}(\mathbf{v}^l)\|_{\mathbf{G}_l^{-1}}$ deviate from the intercept. But more frequently g_{l-1} is small because we are able to generate much more samples at coarse grids as mentioned in subsection 1.1. In this case, we may assume $\hat{f}_{l-1} \approx f_{l-1}$ and therefore $\|\mathbf{f}_l(\mathbf{v}^l) - \hat{\mathbf{f}}_{l-1}(\mathbf{v}^l)\|_{\mathbf{G}_l^{-1}} \approx \|\mathbf{f}_l(\mathbf{v}^l) - \mathbf{f}_{l-1}(\mathbf{v}^l)\|_{\mathbf{G}_l^{-1}} \gg \|\mathbf{f}_{l-1}(\mathbf{v}^l) - \hat{\mathbf{f}}_{l-1}(\mathbf{v}^l)\|_{\mathbf{G}_l^{-1}}$. To be more precise, we make the following first-order expansion:

$$(3.20) \quad \begin{aligned} \|\mathbf{f}_l(\mathbf{v}^l) - \hat{\mathbf{f}}_{l-1}(\mathbf{v}^l)\|_{\mathbf{G}_l^{-1}} &= \|(\mathbf{f}_l(\mathbf{v}^l) - \mathbf{f}_{l-1}(\mathbf{v}^l)) + (\mathbf{f}_{l-1}(\mathbf{v}^l) - \hat{\mathbf{f}}_{l-1}(\mathbf{v}^l))\|_{\mathbf{G}_l^{-1}} \\ &\approx \sqrt{\|\mathbf{f}_l(\mathbf{v}^l) - \mathbf{f}_{l-1}(\mathbf{v}^l)\|_{\mathbf{G}_l^{-1}}^2 + 2\langle \mathbf{f}_{l-1}(\mathbf{v}^l) - \hat{\mathbf{f}}_{l-1}(\mathbf{v}^l), \mathbf{f}_l(\mathbf{v}^l) - \mathbf{f}_{l-1}(\mathbf{v}^l) \rangle_{\mathbf{G}_l^{-1}}} \\ &\approx \|\mathbf{f}_l(\mathbf{v}^l) - \mathbf{f}_{l-1}(\mathbf{v}^l)\|_{\mathbf{G}_l^{-1}} + \frac{\langle \mathbf{f}_{l-1}(\mathbf{v}^l) - \hat{\mathbf{f}}_{l-1}(\mathbf{v}^l), \mathbf{f}_l(\mathbf{v}^l) - \mathbf{f}_{l-1}(\mathbf{v}^l) \rangle_{\mathbf{G}_l^{-1}}}{\|\mathbf{f}_l(\mathbf{v}^l) - \mathbf{f}_{l-1}(\mathbf{v}^l)\|_{\mathbf{G}_l^{-1}}}, \end{aligned}$$

where

$$(3.21) \quad \begin{aligned} &\langle \mathbf{f}_{l-1}(\mathbf{v}^l) - \hat{\mathbf{f}}_{l-1}(\mathbf{v}^l), \mathbf{f}_l(\mathbf{v}^l) - \mathbf{f}_{l-1}(\mathbf{v}^l) \rangle_{\mathbf{G}_l^{-1}} \\ &\leq \left(\frac{1}{M_l} \|\mathbf{f}_{l-1}(\mathbf{v}^l) - \hat{\mathbf{f}}_{l-1}(\mathbf{v}^l)\|_{2,1} \right) \left(M_l \|\mathbf{G}_l^{-1}(\mathbf{f}_l(\mathbf{v}^l) - \mathbf{f}_{l-1}(\mathbf{v}^l))\|_{2,\infty} \right). \end{aligned}$$

Here the $(2, p)$ -norm takes 2-norm on the spatial axis before taking p -norm over the index m of training samples. We note that

$$(3.22) \quad \frac{1}{M_l} \|\mathbf{f}_{l-1}(\mathbf{v}^l) - \hat{\mathbf{f}}_{l-1}(\mathbf{v}^l)\|_{2,1} = \frac{1}{M_l} \sum_{m=1}^{M_l} \|f_{l-1}(v_m^l) - \hat{f}_{l-1}(v_m^l)\|_2$$

is a Monte Carlo estimation of the generalization error g_{l-1} due to the independence of samples $\{(v_m^{l-1}, u_m^{l-1})\}_{m=1}^{M_{l-1}}$ at level $l-1$ and $\{(v_m^l, u_m^l)\}_{m=1}^{M_l}$ at level l . In this way, we justify the estimation

$$(3.23) \quad \|\mathbf{f}_l(\mathbf{v}^l) - \hat{\mathbf{f}}_{l-1}(\mathbf{v}^l)\|_{\mathbf{G}_l^{-1}} \lesssim c_l + \frac{d_l g_{l-1}}{c_l},$$

$$(3.24) \quad c_l = \|\mathbf{f}_l(\mathbf{v}^l) - \mathbf{f}_{l-1}(\mathbf{v}^l)\|_{\mathbf{G}_l^{-1}}, \quad d_l = M_l \|\mathbf{G}_l^{-1}(\mathbf{f}_l(\mathbf{v}^l) - \mathbf{f}_{l-1}(\mathbf{v}^l))\|_{2,\infty}.$$

We note that the coefficients c_l and d_l can be computed without training the network. We further study their growth with respect to M_l in [subsection SM4.3](#) empirically.

3.3.3. Estimating g_l for $2 \leq l \leq L$. As mentioned in [Figure 6](#), we apply [Theorem 3.5](#) in the triangle \mathcal{G}_l to estimate the generalization error g_l from the previously discussed RKHS norm $\|\hat{f}_l - \hat{f}_{l-1}\|_{\mathcal{H}} = \|\mathbf{f}_l(\mathbf{v}^l) - \hat{\mathbf{f}}_{l-1}(\mathbf{v}^l)\|_{\mathbf{G}_l^{-1}}$. We display the correlation between the complexity $\hat{\mathfrak{X}}_2 = 2R\|\mathbf{f}_2(\mathbf{v}^2) - \hat{\mathbf{f}}_1(\mathbf{v}^2)\|_{\mathbf{G}_2^{-1}}/\sqrt{M_2}$ and the generalization error g_2 at level $l=2$ in the example of non-linear Schrödinger equation in [Figure 8](#).

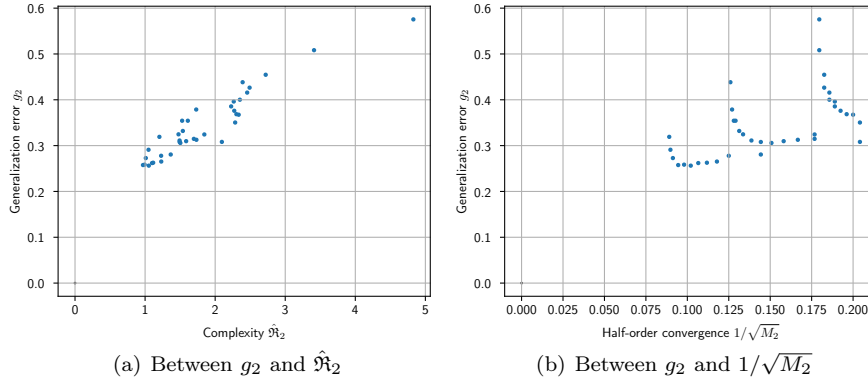


FIG. 8. Correlation between the generalization error g_2 and the complexity $\hat{\mathfrak{X}}_2$ in the triangle \mathcal{G}_2 of [Figure 6](#). Detailed discussion on the computation is presented in [section SM4](#). We note the importance of the RKHS norm $\|\mathbf{f}_2(\mathbf{v}^2) - \hat{\mathbf{f}}_1(\mathbf{v}^2)\|_{\mathbf{G}_2^{-1}}$: if we leave it out in $\hat{\mathfrak{X}}_2$ and turn to consider $1/\sqrt{M_2}$, we observe less correlation in (b) compared to (a).

We can still witness the linear correlation in [Figure 8 \(a\)](#) during fine-tuning (cf. [Figure 7 \(a\)](#)). Similar to the case of g_1 , using the estimation to the RKHS norm [\(3.23\)](#), we consider the *a priori* estimator to g_l with coefficients [\(3.24\)](#):

$$(3.25) \quad \hat{g}_l = \frac{2R}{\sqrt{M_l}} \left(c_l + \frac{d_l \hat{g}_{l-1}}{c_l} \right).$$

For the non-linear Schrödinger equation problem, we consider MLFT with $L=2$ levels as mentioned in [subsection 1.1](#). The *a priori* estimators to the generalization error in approximating the coarse-grid and fine-grid solvers at level $l=1$ and $l=2$ are respectively

$$(3.26) \quad \hat{g}_1 = \frac{2Rc_1}{\sqrt{M_1}}, \quad \hat{g}_2 = \frac{2R}{\sqrt{M_2}} \left(c_2 + \frac{2d_2 R c_1}{c_2 \sqrt{M_1}} \right),$$

where c_1, R are computed from [\(3.19\)](#) and c_2, d_2 computed from [\(3.24\)](#).

3.4. A *posteriori* error estimator. It is well known that *a priori* error estimation may be pessimistic, especially in estimating the generalization of neural networks [47, 6]. Moreover, poor estimation may give poor solutions to the budget distribution problem (1.6). Additionally, validity of the infinite-width NTK theory is questioned in finite-width scenarios which are mostly the case in practice [1, 28]. Hence, we may try to build practical *a posteriori* error estimator to the generalization error g_L in approximating the finest-grid solver f_L . Combining theoretical insights and empirical observations, the *a posteriori* error estimator may provide useful information about the generalization error for the budget distribution problem (1.6). The *a posteriori* error estimator may also extend to finite-width cases which are not solidly covered by the infinite-width NTK theory. In detail, we substitute the coefficients R , c_l and d_l in (3.19) and (3.25) by variables a_l and b_l :

$$(3.27) \quad \hat{g}_1 = \frac{a_1}{\sqrt{M_1}}, \quad \hat{g}_l = \frac{a_l}{\sqrt{M_l}} (b_l + \hat{g}_{l-1}), \quad 2 \leq l \leq L.$$

We find values of the variables a_l and b_l *a posteriori* from trials performing MLFT with different combinations of M_l . By introducing a validation set, we compute the generalization error g_l at the trials. One particular method is the least square method: we fit a_l and b_l by minimizing the MSE between $\log g_L$ and $\log \hat{g}_L$ over trials. The least square method needs at least L trials to determine the function $\hat{g}_L(M_1, M_2, \dots, M_L)$. We also propose a heuristic method using only one trial of MLFT by setting $2L - 1$ equations: we set $b_l = \mathbb{E}_{v \sim \mathcal{D}} \|f_l(v) - f_{l-1}(v)\|_2$ and $g_l = \hat{g}_l$. The motivation to set b_l follows from the inequality in the triangle \mathcal{C}_l of Figure 6 that $\|f_l(v) - \hat{f}_{l-1}(v)\|_2 \leq \|f_l(v) - f_{l-1}(v)\|_2 + \|f_{l-1}(v) - \hat{f}_{l-1}(v)\|_2$. For ML2MC [44], the *a posteriori* error estimator has the form $\hat{g}_L = \sum_{l=1}^L a_l / \sqrt{M_l}$. The variables a_l can also be found by the heuristic method: we set L equations equating the computed and the estimated generalization error at each level.

In the case of the non-linear Schrödinger equation problem, we have $L = 2$ and

$$(3.28) \quad \hat{g}_2^{\text{MLFT}}(M_1, M_2) = \frac{a_2}{\sqrt{M_2}} \left(b_2 + \frac{a_1}{\sqrt{M_1}} \right), \quad \hat{g}_2^{\text{ML2MC}}(M_1, M_2) = \frac{a_1}{\sqrt{M_1}} + \frac{a_2}{\sqrt{M_2}}.$$

After determining values of the variables, one may solve the budget distribution problem (1.6) to optimize the number of training samples M_l at each level. Here the optimal M_l for ML2MC can be directly found by the Cauchy-Schwarz inequality, while the problem for MLFT is a little harder. However, we note that $1/\sqrt{\prod_{l'=1}^l M_{l'}}$ is convex with respect to (M_1, M_2, \dots, M_L) for $1 \leq l \leq L$, so highly efficient solvers can be deployed to solve the problem (1.6).

4. Numerical results. We conduct numerical experiments to show the performance of MLFT and compare between algorithms. We tackle problems with oscillations, discontinuities, or rough coefficients. For these problems, the finest-grid solvers contain much detail. Hence, it poses challenges for the regression network to have a small generalization error when there is a limited budget for generating training samples.

We first implement the neural networks in PyTorch [49] and then migrate to JAX [12] and Stax [13] in order to use the package Neural Tangents [48] to calculate NTK. The codes of experiments were run on Nvidia Tesla K80. We separately generate three sets of samples for training, validation, and testing respectively according to the procedure described in subsection 2.1. The generalization errors to construct the

a posteriori error estimator are computed on the validation set, while the reported errors (2.3) and (2.4) in figures are computed on the testing set. The batch size of 32 is used for all the experiments. We fix the seed of random batch and random initialization for better comparison. We train the network for 10 000 iterations at each level, when we observe that the training error is smaller than the testing error (e.g., in Figures 1, 11 and 14).

4.1. Non-linear Schrödinger equation with oscillatory potentials. We first consider the example of one-dimensional non-linear Schrödinger equation, or namely the Gross–Pitaevskii equation. This equation relates to Bose–Einstein condensation [3, 8] and receives emerging research attention [31]. As already introduced in subsection 1.1, we consider the equation (1.1) and (1.2) on domain $\Omega = [0, 1]$ with periodic boundary condition. The solution map we are interested in is the potential-ground state map.

We set the dispersion coefficient to be $\beta = 100$. The distribution \mathcal{D} of potential v is generated by

$$(4.1) \quad v(x) = \sum_{k=1}^K A_k (\alpha + \cos(2\pi\omega_k x + \phi_k)) \frac{1}{\sqrt{2\pi}\sigma_k} \exp\left(-\frac{d(x, c_k)^2}{2\sigma_k^2}\right), \quad x \in [0, 1]$$

where $d(x, y) = x - y - \lfloor x - y + 1/2 \rfloor \in [-1/2, 1/2)$. We set $K = 4$, $\alpha = 0.1$, and sample $A_k \sim \mathcal{U}[-400, -200]$, $\omega_k \sim \mathcal{U}[40, 80]$, $1/\sigma_k \sim \mathcal{U}[10, 20]$, and $\phi_k \sim \mathcal{U}[0, 2\pi]$ independently. The ground state u is calculated by the gradient flow solver described in [9] with time step $\tau = 1$.

As mentioned in subsection 1.1, we consider $L = 2$ levels with grid steps $h_1 = 1/N_1 = 1/40$ and $h_2 = 1/N_2 = 1/320$ respectively. From the visualization of potential-ground state pair in Figure 1, we notice that large high-frequency components of the potential v produce small oscillations in the ground state u . Hence, we select $R_{2 \rightarrow 1} : \mathcal{V}_2 \rightarrow \mathcal{V}_1$ to be Fourier restriction operator since the frequency of oscillations in the potential v exceeds the Nyquist frequency of the coarse grid. On the coarse grid only low-frequency components of the potential v remain, and we select $I_{1 \rightarrow 2} : \mathcal{U}_1 \rightarrow \mathcal{U}_2$ to be the cubic interpolation operator. We observe that running times of coarse-grid and fine-grid solvers approximately satisfy $t_2 = 64t_1$, as discussed in subsection SM3.1.

We use the MNN- \mathcal{H} network [19] as the regression network. We use a network with 6 branches where each branch is a 5-layer 160-channel sub-network as specified in section SM2. We use Momentum [53] as the optimizer with momentum coefficient 0.975 and learning rate 10. The theory of NTK is proved to be applicable for the Momentum optimizer [40]. The learning rate is seemingly huge but is applicable in the NTK parameterization [32].

Recall that M_1 and M_2 are the numbers of training samples generated by the coarse-grid and fine-grid solvers f_1 and f_2 respectively. We aim to reduce the generalization error g_2 under a fixed budget for generating training samples, i.e., $M_1 t_1 + M_2 t_2 = T$. To explore different combinations of M_1 and M_2 under a fixed budget T , we define the coarse-to-total ratio $r = M_1 t_1 / (M_1 t_1 + M_2 t_2)$ to be the proportion of budget spent in generating coarse-grid samples. We examine the relationship between the error g_2 (2.3) and (2.4) and the coarse-to-total ratio r under a budget fixed T in Figure 9. We also plot the error estimators \hat{g}_2 to the generalization error introduced in subsections 3.3 and 3.4. The heuristic method to construct the *a posteriori* error estimator runs a trial of MLFT with $M_1 = 64$ coarse-grid samples and $M_2 = 32$ fine-grid samples.

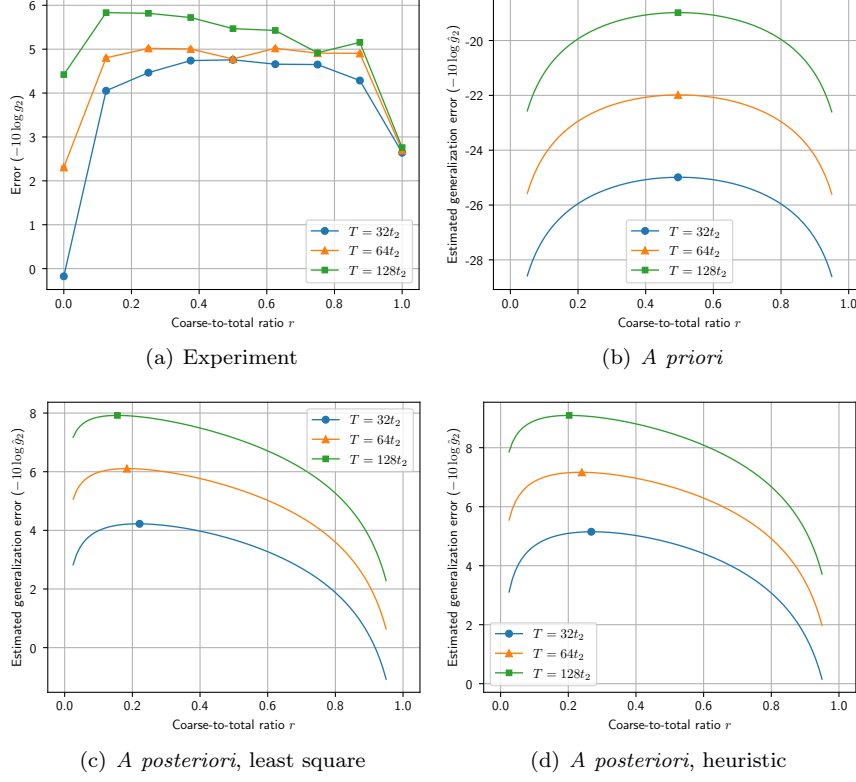


FIG. 9. Error g_2 (2.3) and (2.4) and the estimated generalization error \hat{g}_2 for the non-linear Schrödinger equation problem. In experiments (a) when $r = 0$ we use only fine-grid samples to train the regression network (i.e., single-level $l = 2$) and when $r = 1$ we use only coarse-grid samples (i.e., single-level $l = 1$). We observe that MLFT with a selected r is able to outperform single-level training with either $l = 1$ or 2 . In particular, combination of $T = 32t_2$ and $r = 1/2$ has smaller generalization error than $T = 128t_2$ and $r = 0$. This means that MLFT achieves the same generalization error while saving 75% of the budget for generating training samples. For error estimators, we observe that the a priori error estimator (b) is pessimistic. The a posteriori error estimators capture the generalization error better. The r with the smallest estimated generalization error is marked, as the solution to the budget distribution problem (1.6). A significant reduction of generalization error is still presented in experiments with these r optimized from a posteriori error estimators.

From the experiment, we observe that MLFT provides a significant reduction of the generalization error in approximating the fine-grid solver with a regression network. The margin is larger when we are given smaller budget for generating training samples. We notice that the r with the smallest estimated generalization error decreases when the budget grows. The a posteriori error estimators correctly capture this tendency of decreasing r .

4.2. Viscous Burgers' equation with discontinuous initial values. Burgers' equation plays an essential role in fluid dynamics and traffic flow modeling. Since the viscous Burgers' equation contains both diffusion and non-linear convection terms, it is frequently taken as an example for conservation law solvers and model reduction

methods [41]. The one-dimensional viscous Burgers' equation for $u(x; t)$ is

$$(4.2) \quad u_t + \left(\frac{u^2}{2} \right)_x = \kappa u_{xx}, \quad x \in \Omega.$$

We consider the equation on $\Omega = [0, 1]$ with a periodic boundary condition. The solution map we are approximating is the time evolution map. Formally, we are interested in the solution map $v \mapsto u_v$ which takes initial value $v = u(\cdot; 0)$ as parameter and gives terminal value $u_v = u(\cdot; t_{\text{term}})$ as solution.

We consider the problem with discontinuous initial values. In detail, the distribution \mathcal{D} of parameter v consists of step functions

$$(4.3) \quad v(x) = \sum_{k=1}^K A_k \chi_{[(k-1)/K, k/K)}(x), \quad x \in [0, 1].$$

We set K to be 40 and sample $A_k \sim \mathcal{N}(0, 1)$ independently for $1 \leq k \leq K$. We consider the solution at terminal time $t_{\text{term}} = 0.1$ under diffusivity coefficient $\kappa = 0.005$. For the numerical solver F_l at each level, we use the first-order operator splitting scheme which includes Godnov scheme for convection and the explicit Euler scheme for diffusion. Due to stability reasons, we choose the time step to be $10h^2$ on the grid with grid step h . As a result, the time to run the level- l solver satisfies $t_l \propto 1/h_l^3$. We choose the average operator to be $R_{L \rightarrow l} : \mathcal{V}_L \rightarrow \mathcal{V}_l$, and the linear interpolation operator to be $I_{l \rightarrow L} : \mathcal{U}_l \rightarrow \mathcal{U}_L$.

We consider MLFT with $L = 2$ levels with grid steps $h_1 = 1/N_1 = 1/80$ and $h_2 = 1/N_2 = 1/320$. In this case, $t_2 = 64t_1$. We visualize a training sample, namely an initial value-terminal value pair in Figure 10. We use a 9-layer convolutional neural network with 160 channels as the regression network, as specified in section SM2. We use the Momentum optimizer with learning rate 10 and momentum coefficient 0.975. In this problem, MLFT still reduces the generalization error in approximating the fine-grid solver as shown in Figure 11. We compute the error g_2 (2.3) and (2.4) of MLFT and ML2MC with different coarse-to-total ratio r under a fixed budget T . We also plot the estimated generalization error \hat{g}_2 of the *a posteriori* estimator constructed by the heuristic method which runs a trial of MLFT with $M_1 = 64$ coarse-grid samples and $M_2 = 32$ fine-grid samples.

From the experiments, we find that both MLFT and ML2MC reduces the generalization error g_2 in approximating the finest-grid solver f_2 . In the case that the budget for generating training samples is small, MLFT reduces the generalization error slightly better than ML2MC. Besides, we find that at the fine level $l = 2$ ML2MC converges much slower than MLFT. This is because of the effect of curriculum learning [61] as mentioned in Algorithm 2.3. In MLFT, the convergence of fine-tuning steps is boosted by the previous training or fine-tuning steps. However, in ML2MC, networks are trained separately and converge separately.

4.3. Diagonal of inverse to elliptic operators with rough coefficients.

The inverse to an elliptic operator is known as the Green function, which serves as the fundamental solution to elliptic PDE. As an example, we are particularly interested in the diagonal of inverse $u(\mathbf{x}) = g(\mathbf{x}, \mathbf{x})$ to the Schrödinger operator, namely $g = (-\Delta + v)^{-1}$. This problem has been studied in [43, 21] and has applications in quantum chemistry. We aim to approximate the potential-diagonal of inverse map of the Schrödinger operator, which takes potential $v(\mathbf{x})$ as parameter and gives the diagonal of inverse $u_v(\mathbf{x}) = u(\mathbf{x})$ to the corresponding Schrödinger operator.

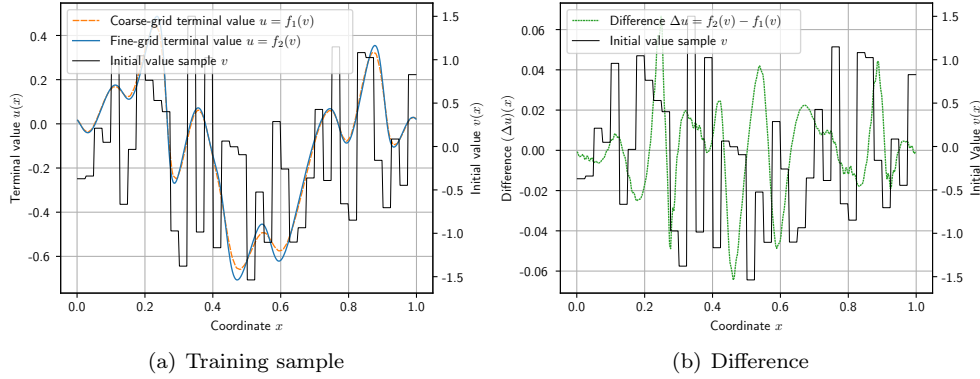


FIG. 10. Visualization of a training sample of the viscous Burgers' equation problem. The coarse-grid sample suffers from numerical dissipation as shown in (a), which causes the difference between coarse-grid and fine-grid samples in (b).

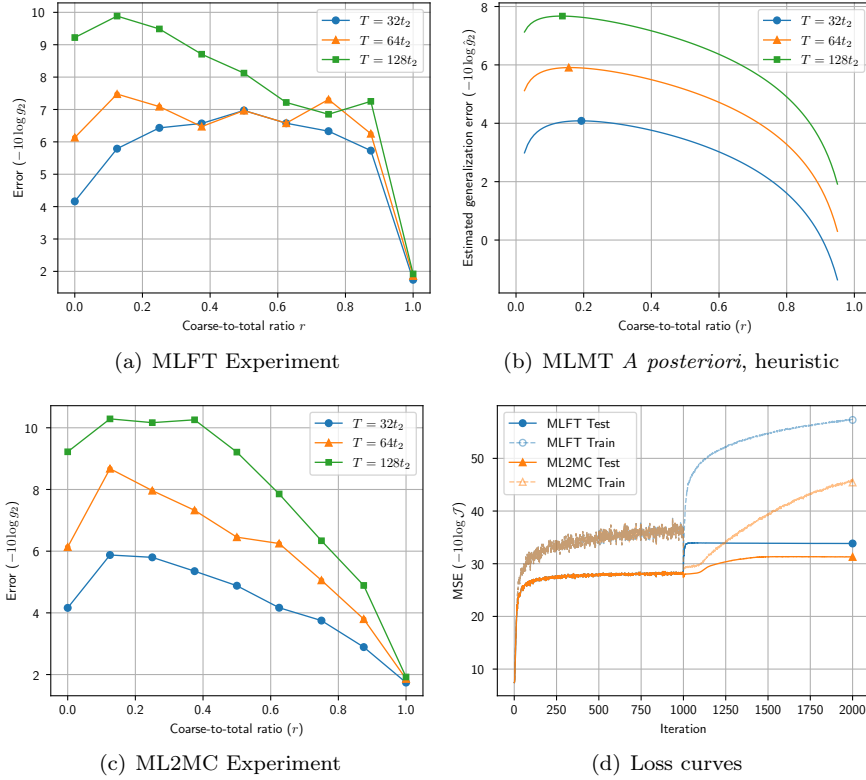


FIG. 11. Error g_2 (2.3) and (2.4) and the estimated generalization error \hat{g}_2 for the viscous Burgers' equation problem. We observe that in experiments (a) the combination of $T = 32t_2$ and $r = 1/2$ with MLFT has smaller generalization error than $T = 64t_2$ and $r = 0$, achieving a 50% saving of the budget. The a posteriori error estimator (b) captures the trend of error curves in (a). In comparison between MLFT and ML2MC in (c), we observe that MLFT reduces the generalization error slightly better than ML2MC in the case $T = 32t_2$, namely when the budget is small. We plot the loss curves of MLFT and ML2MC in the case $M_1 = 1024$ and $M_2 = 16$ in (d), and find that at level $l = 2$ MLFT converges much faster (in less than 500 iterations) than ML2MC (in about 5000 iterations).

Let us tackle the two-dimensional problem with $\mathbf{x} = (x, y)$ on $\Omega = [0, 1]^2$ with a periodic boundary condition. We generate rough potentials v by

$$(4.4) \quad v(x, y) = \sum_{k=1}^K A_k \cos(2^k \pi(x + y) + \phi_k) + \sum_{k=1}^K B_k \cos(2^k \pi(2x - y) + \psi_k) + C.$$

For the distribution \mathcal{D} of rough potentials, we set $K = 6$, $C = 100$ and sample $A_k, B_k \sim \mathcal{N}(0, 20^2)$ and $\phi_k, \psi_k \sim \mathcal{U}[0, 2\pi]$ independently. We visualize a potential-diagonal of inverse pair in Figure 12. We invoke the SelInv algorithm [43] for the numerical solvers F_l , which takes $O(1/h^3)$ times on a two-dimensional grid with grid step $h = 1/N$. We choose $R_{L \rightarrow l} : \mathcal{V}_L \rightarrow \mathcal{V}_l$ to be the Fourier restriction operator, and $I_{l \rightarrow L} : \mathcal{U}_l \rightarrow \mathcal{U}_L$ to be the cubic interpolation operator.

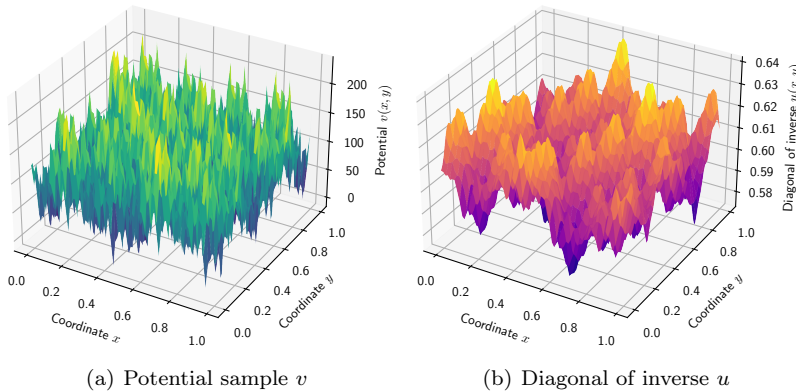


FIG. 12. Visualization of a training sample of the diagonal of inverse problem. We observe high-frequency oscillations in the potential v (a), but the diagonal of the inverse u to the corresponding Schrödinger operator (b) is smoother.

We consider four different grids with grid step $h_1 = 1/N_1 = 1/10$, $h_2 = 1/N_2 = 1/20$, $h_3 = 1/N_3 = 1/40$, and $h_4 = 1/N_4 = 1/80$ respectively. In this case, $t_4 = 8t_3 = 64t_2 = 512t_1$. We aim to approximate the finest-grid solver f_4 on the finest grid with grid step $h_4 = 1/80$. We use a two-dimensional MNN- \mathcal{H} network with 4 branches and 5 layers as the regression network, as specified in section SM2. We use the Adam optimizer with learning rate 3.0×10^{-4} [38]. Although the theory of NTK is not applicable in this case, we still consider the ability of MLFT in reducing the generalization error. We perform MLFT with different number of levels L for $1 \leq L \leq 4$: we successively use training samples generated at the grid with grid step h_{4+l-L} for $l = 1, 2, \dots, L$. The number of training samples M_l at different levels are optimized according to the budget distribution problem (1.6). Here we use the *a posteriori* error estimator constructed by the heuristic method which runs trials with $M_1 = 256$, $M_2 = 128$, $M_3 = 64$ and $M_4 = 32$. We compute and report the testing error g_4^{test} with different numbers of levels L under a fixed budget T in Figure 13. We observe that as the number of levels grows, MLFT achieves smaller error in approximating the finest-grid solver under a fixed budget for generating training samples.

We compare MLFT and ML2MC with $L = 4$ levels under different budgets T for generating training samples in Figure 14. We compute the testing error g_4^{test} to compare the accuracy of MLFT and ML2MC. We also plot the loss curves in order to understand the convergence and compare the efficiency. For reference, we show the

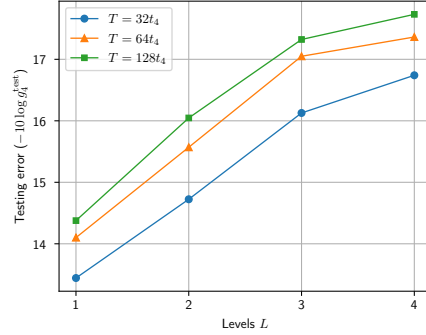


FIG. 13. Testing error g_4^{test} for the diagonal of inverse problem. We observe that the error is significantly reduced under a fixed budget T when the number of levels increases.

optimized number of training samples at different levels in Table 1 as the solution to the budget distribution problem (1.6).

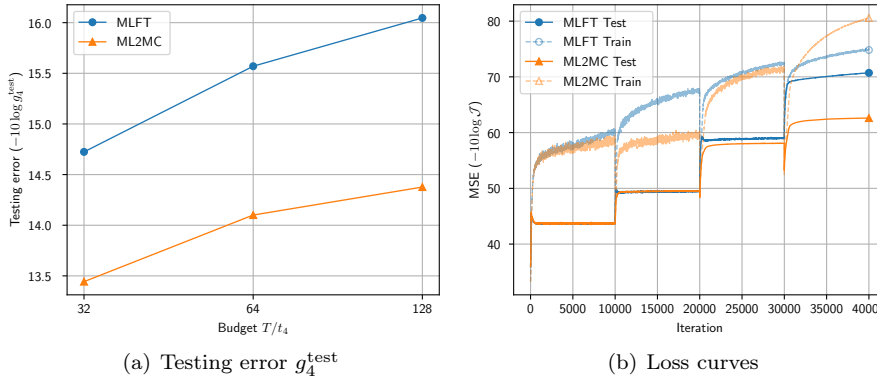


FIG. 14. Comparison between MLFT and ML2MC for the diagonal of inverse problem. In terms of accuracy (a), we observe that MLFT reduces the generalization error better than ML2MC. In terms of convergence (b), we observe that MLFT converges faster than ML2MC at the level $l = 3$. We note that the difference between MLFT and ML2MC becomes larger after entering level $l = 4$. This is because MLFT corrects the generalization error in fine-tuning steps while ML2MC accumulates the generalization error. The loss curves are extracted from the experiments in (a) under the fixed budget $T = 32t_4$.

5. Conclusion. We establish the Multi-Level Fine-Tuning (MLFT) algorithm Algorithm 2.2 in this paper. We aim to reduce the generalization error of regression networks in approximating solution maps and numerical solvers without spending more time in generating training samples. Inspired by the resemblance between fine-tuning techniques and multi-scale methods, we train the regression networks on samples generated at the coarse grid and fine-tune on samples generated at finer grids. In experiments, we achieve significant reduction of the generalization error with MLFT under a fixed budget for generating training samples, compared with base-lines trained with only coarse-grid or only fine-grid samples. Thanks to the Neural Tangent Kernel (NTK) theory, we are able to perform analysis on the MLFT algorithm under assumptions. Although it is notoriously difficult to find sharp bounds on the generalization error of neural networks, we make use of the form of generalization error

TABLE 1

Optimized number of training samples at different levels for the diagonal of inverse problem. The number of training samples is found by solving the budget distribution problem (1.6) and is subject to $M_1t_1 + M_2t_2 + M_3t_3 + M_4t_4 = T$ or $M_1/512 + M_2/64 + M_3/8 + M_4 = T/t_4$. We observe that compared to MLFT, ML2MC generates much more coarse-grid samples in exchange of some fine-grid samples.

	T/t_4	M_1	M_2	M_3	M_4
MLFT Algorithm 2.2	32	53	51	46	25
	64	68	72	76	53
	128	86	101	126	111
ML2MC Algorithm 2.3	32	2143	653	54	7
	64	4286	1305	107	13
	128	8572	2611	214	27

provided by statistical machine learning theory and find the coefficients *a posteriori*. By minimizing the estimated generalization error given by the practical *a posteriori* error estimator, we distribute the budget for generating training samples over levels. In this way, we hope to provide practical guidance to reduce the generalization error with theoretical insight.

We have not exhaustively tested MLFT on many other intriguing numerical problems in scientific machine learning. Problems with heavier scaling of time with respect to the grid step may enjoy greater reduction of generalization error with the help of MLFT. It is also possible to generalize MLFT to other settings besides regression networks. For the error estimators, we are interested in other methods to construct the *a posteriori* error estimators besides the two mentioned in the paper. More detailed analysis can be done, possibly providing new forms of the generalization error.

6. Acknowledgements. We would like to thank Tianle Cai for providing reference. We also appreciate the discussion with Professor Bin Dong on the delivery of the subject. We would like to express our gratitude to the anonymous reviewers together with Yiqing Xie, Weijie Chen, Jikai Hou, and Zeyu Zhao for careful proofreading and kind comments on the manuscript, which greatly improves the quality of the paper.

REFERENCES

- [1] Z. ALLEN-ZHU, Y. LI, AND Y. LIANG, *Learning and generalization in overparameterized neural networks, going beyond two layers*, in Advances in Neural Information Processing Systems, vol. 32, Vancouver, Canada, 2019, Curran Associates, pp. 6158–6169.
- [2] Z. ALLEN-ZHU, Y. LI, AND Z. SONG, *A convergence theory for deep learning via overparameterization*, in Proceedings of the 36th International Conference on Machine Learning, Long Beach, CA, 2019, PMLR, pp. 242–252.
- [3] J. R. ANGLIN AND W. KETTERLE, *Bose–Einstein condensation of atomic gases*, Nature, 416 (2002), pp. 211–218, <https://doi.org/10.1038/416211a>.
- [4] S. ARORA, S. DU, W. HU, Z. LI, AND R. WANG, *Fine-grained analysis of optimization and generalization for overparameterized two-layer neural networks*, in Proceedings of the 36th International Conference on Machine Learning, Long Beach, CA, 2019, PMLR, pp. 322–332.
- [5] S. ARORA, S. S. DU, W. HU, Z. LI, R. R. SALAKHUTDINOV, AND R. WANG, *On Exact Computation with an Infinitely Wide Neural Net*, in Advances in Neural Information Processing Systems, vol. 32, Vancouver, Canada, 2019, Curran Associates, pp. 8141–8150.

- [6] S. ARORA, R. GE, B. NEYSHABUR, AND Y. ZHANG, *Stronger generalization bounds for deep nets via a compression approach*, in Proceedings of the 35th International Conference on Machine Learning, Stockholm, Sweden, 2018, PMLR, pp. 254–263.
- [7] S. ARRIDGE, P. MAASS, O. ÖKTEM, AND C.-B. SCHÖNLIEB, *Solving inverse problems using data-driven models*, Acta Numer., 28 (2019), pp. 1–174, <https://doi.org/10.1017/S0962492919000059>.
- [8] V. S. BAGNATO, D. J. FRANTZESKAKIS, P. G. KEVREKIDIS, B. A. MALOMED, AND D. MIHALACHE, *Bose–Einstein condensation: Twenty years after*, Rom. Rep. Phys., 67 (2015), pp. 5–50.
- [9] W. BAO AND Q. DU, *Computing the ground state solution of Bose–Einstein condensates by a normalized gradient flow*, SIAM J. Sci. Comput., 25 (2004), pp. 1674–1697, <https://doi.org/10.1137/S1064827503422956>.
- [10] P. L. BARTLETT AND S. MENDELSON, *Rademacher and Gaussian complexities: Risk bounds and structural results*, in Computational Learning Theory. COLT 2001. Lecture Notes in Computer Science, vol. 2111, Amsterdam, The Netherlands, 2001, Springer, Berlin, Heidelberg, pp. 224–240, https://doi.org/10.1007/3-540-44581-1_15.
- [11] M. BELKIN, S. MA, AND S. MANDAL, *To understand deep learning we need to understand kernel learning*, in Proceedings of the 35th International Conference on Machine Learning, Stockholm, Sweden, 2018, PMLR, pp. 541–549.
- [12] J. BRADBURY, R. FROSTIG, P. HAWKINS, M. J. JOHNSON, C. LEARY, D. MACLAURIN, G. NECULA, A. PASZKE, J. VANDERPLAS, S. WANDERMAN-MILNE, AND Q. ZHANG, *JAX: composable transformations of Python+NumPy programs*, 2018, <http://github.com/google/jax>.
- [13] J. BRADBURY, R. FROSTIG, P. HAWKINS, M. J. JOHNSON, C. LEARY, D. MACLAURIN, G. NECULA, A. PASZKE, J. VANDERPLAS, S. WANDERMAN-MILNE, AND Q. ZHANG, *Stax, a flexible neural net specification library in JAX*, 2018, <https://github.com/google/jax/blob/master/jax/experimental/stax.py>.
- [14] Y. CAO AND Q. GU, *Generalization bounds of stochastic gradient descent for wide and deep neural networks*, in Advances in Neural Information Processing Systems, vol. 32, Vancouver, Canada, 2019, Curran Associates, pp. 10836–10846.
- [15] Y. CAO AND Q. GU, *Generalization error bounds of gradient descent for learning over-parameterized deep ReLU networks*, Proc. AAAI Conf. Artif. Intell., 34 (2020), pp. 3349–3356, <https://doi.org/10.1609/aaai.v34i04.5736>.
- [16] C. CORTES, M. KLOFT, AND M. MOHRI, *Learning kernels using local Rademacher complexity*, in Advances in Neural Information Processing Systems, vol. 26, Lake Tahoe, NV, 2013, Curran Associates, Inc., pp. 2760–2768.
- [17] W. E AND B. ENGQUIST, *The heterogenous multiscale methods*, Commun. Math. Sci., 1 (2003), pp. 87–132.
- [18] W. E AND B. YU, *The Deep Ritz Method: A deep learning-based numerical algorithm for solving variational problems*, Commun. Math. Stat., 6 (2018), pp. 1–12, <https://doi.org/10.1007/s40304-018-0127-z>.
- [19] Y. FAN, J. FELIU-FABÀ, L. LIN, L. YING, AND L. ZEPEDA-NÚÑEZ, *A multiscale neural network based on hierarchical nested bases*, Res. Math. Sci., 6 (2019), 21, <https://doi.org/10.1007/s40687-019-0183-3>.
- [20] Y. FAN, L. LIN, L. YING, AND L. ZEPEDA-NÚÑEZ, *A multiscale neural network based on hierarchical matrices*, Multiscale Model. Simul., 17 (2019), pp. 1189–1213, <https://doi.org/10.1137/18M1203602>.
- [21] Y. FAN, C. OROZCO BOHORQUEZ, AND L. YING, *BCR-Net: A neural network based on the nonstandard wavelet form*, J. Comput. Phys., 384 (2019), pp. 1–15, <https://doi.org/10.1016/j.jcp.2019.02.002>.
- [22] Y. FAN AND L. YING, *Solving optical tomography with deep learning*, preprint, arXiv:1910.04756 [physics.comp-ph], (2019), <https://arxiv.org/abs/1910.04756>.
- [23] Y. FAN AND L. YING, *Solving electrical impedance tomography with deep learning*, J. Comput. Phys., 404 (2020), 109119, <https://doi.org/10.1016/j.jcp.2019.109119>.
- [24] R. GAO, Y. LU, J. ZHOU, S.-C. ZHU, AND Y. N. WU, *Learning generative ConvNets via multi-grid modeling and sampling*, in Proceedings of the IEEE Conference on Computer Vision and Pattern Recognition (CVPR), Salt Lake City, UT, 2018, IEEE, pp. 9155–9164, <https://doi.org/10.1109/CVPR.2018.00954>.
- [25] M. B. GILES, *Multilevel Monte Carlo path simulation*, Oper. Res., 56 (2008), pp. 607–617, <https://doi.org/10.1287/opre.1070.0496>.
- [26] D. GILTON, G. ONGIE, AND R. WILLETT, *Neumann networks for linear inverse problems in imaging*, IEEE Trans. Comput. Imaging, 6 (2020), pp. 328–343, <https://doi.org/10.1109/>

- [TCI.2019.2948732](#).
- [27] E. HABER, L. RUTHOTTO, E. HOLTHAM, AND S.-H. JUN, *Learning across scales — Multi-scale methods for convolution neural networks*, in Proceedings of the Thirty-Second AAAI Conference on Artificial Intelligence (AAAI-18), New Orleans, LA, 2018, AAAI Press, pp. 3142–3148.
- [28] B. HANIN AND M. NICA, *Finite depth and width corrections to the neural tangent kernel*, in 8th International Conference on Learning Representations, ICLR 2020, Addis Ababa, Ethiopia, 2020, <https://openreview.net/forum?id=SJgndT4KwB>.
- [29] T. HOFMANN, B. SCHÖLKOPF, AND A. J. SMOLA, *Kernel methods in machine learning*, Ann. Statist., 36 (2008), pp. 1171–1220, <https://doi.org/10.1214/009053607000000677>.
- [30] M. HUH, P. AGRAWAL, AND A. A. EFROS, *What makes ImageNet good for transfer learning?*, preprint, arXiv:1608.08614 [cs.CV], (2016), <http://arxiv.org/abs/1608.08614>.
- [31] B. ILAN AND M. I. WEINSTEIN, *Band-edge solitons, nonlinear Schrödinger/Gross–Pitaevskii equations, and effective media*, Multiscale Model. Simul., 8 (2010), pp. 1055–1101, <https://doi.org/10.1137/090769417>.
- [32] A. JACOT, F. GABRIEL, AND C. HONGLER, *Neural Tangent Kernel: Convergence and generalization in neural networks*, in Advances in Neural Information Processing Systems, vol. 31, Montreal, Canada, 2018, Curran Associates, pp. 8571–8580.
- [33] H. JUNCAI AND X. JINCHAO, *MgNet: A unified framework of multigrid and convolutional neural network*, Sci. China Math., 62 (2019), pp. 1331–1354, <https://doi.org/10.1007/s11425-019-9547-2>.
- [34] Y. KHOO, J. LU, AND L. YING, *Solving for high-dimensional committor functions using artificial neural networks*, Res. Math. Sci., 6 (2018), 1, <https://doi.org/10.1007/s40687-018-0160-2>.
- [35] Y. KHOO, J. LU, AND L. YING, *Solving parametric PDE problems with artificial neural networks*, European J. Appl. Math., (2020), <https://doi.org/10.1017/S0956792520000182>.
- [36] Y. KHOO AND L. YING, *SwitchNet: A neural network model for forward and inverse scattering problems*, SIAM J. Sci. Comput., 41 (2019), pp. A3182–A3201, <https://doi.org/10.1137/18M1222399>.
- [37] B. KIM, V. C. AZEVEDO, N. THUEREY, T. KIM, M. GROSS, AND B. SOLENTHALER, *Deep Fluids: A generative network for parameterized fluid simulations*, Comput. Graph. Forum, 38 (2019), pp. 59–70, <https://doi.org/10.1111/cgf.13619>.
- [38] D. P. KINGMA AND J. BA, *Adam: A method for stochastic optimization*, in 3rd International Conference on Learning Representations, ICLR 2015, Conference Track Proceedings, San Diego, CA, 2015, <http://arxiv.org/abs/1412.6980>.
- [39] I. LAGARIS, A. LIKAS, AND D. FOTIADIS, *Artificial neural networks for solving ordinary and partial differential equations*, IEEE Trans. Neural Netw. Learn. Syst., 9 (1998), pp. 987–1000, <https://doi.org/10.1109/72.712178>.
- [40] J. LEE, L. XIAO, S. SCHOENHOLZ, Y. BAHRI, R. NOVAK, J. SOHL-DICKSTEIN, AND J. PENNINGTON, *Wide neural networks of any depth evolve as linear models under gradient descent*, in Advances in Neural Information Processing Systems, vol. 32, Vancouver, Canada, 2019, Curran Associates, pp. 8572–8583.
- [41] K. LEE AND K. T. CARLBERG, *Model reduction of dynamical systems on nonlinear manifolds using deep convolutional autoencoders*, J. Comput. Phys., 404 (2020), 108973, <https://doi.org/10.1016/j.jcp.2019.108973>.
- [42] T. LIANG AND A. RAKHLIN, *Just interpolate: Kernel “Ridgeless” regression can generalize*, Ann. Statist., 48 (2020), pp. 1329–1347, <https://doi.org/10.1214/19-AOS1849>.
- [43] L. LIN, J. LU, L. YING, R. CAR, AND W. E, *Fast algorithm for extracting the diagonal of the inverse matrix with application to the electronic structure analysis of metallic systems*, Commun. Math. Sci., 7 (2009), pp. 755–777.
- [44] K. O. LYE, S. MISHRA, AND R. MOLINARO, *A multi-level procedure for enhancing accuracy of machine learning algorithms*, European J. Appl. Math., (2020), <https://doi.org/10.1017/S0956792520000224>.
- [45] A. MAURER, *The Rademacher complexity of linear transformation classes*, in Learning Theory. COLT 2006. Lecture Notes in Computer Science, vol. 4005, Pittsburgh, PA, 2006, Springer, Berlin, Heidelberg, pp. 65–78, https://doi.org/10.1007/11776420_8.
- [46] M. MOHRI, A. ROSTAMIZADEH, AND A. TALWALKAR, *Foundations of machine learning*, MIT Press, Cambridge, MA, 2 ed., 2018.
- [47] B. NEYSHABUR, S. BHOJANAPALLI, D. MCALLESTER, AND N. SREBRO, *Exploring generalization in deep learning*, in Advances in Neural Information Processing Systems, vol. 30, Long Beach, CA, 2017, Curran Associates, pp. 5947–5956.
- [48] R. NOVAK, L. XIAO, J. HRON, J. LEE, A. A. ALEMI, J. SOHL-DICKSTEIN, AND S. S.

- SCHOENHOLZ, *Neural Tangents: Fast and easy infinite neural networks in Python*, in 8th International Conference on Learning Representations, ICLR 2020, Addis Ababa, Ethiopia, 2020, <https://openreview.net/forum?id=SkID9yrFPS>.
- [49] A. PASZKE, S. GROSS, F. MASSA, A. LERER, J. BRADBURY, G. CHANAN, T. KILLEEN, Z. LIN, N. GIMELSHEIN, L. ANTIGA, A. DESMAISON, A. KOPF, E. YANG, Z. DEVITO, M. RAISON, A. TEJANI, S. CHILAMKURTHY, B. STEINER, L. FANG, J. BAI, AND S. CHINTALA, *PyTorch: An imperative style, high-performance deep learning library*, in Advances in Neural Information Processing Systems, vol. 32, Vancouver, Canada, 2019, Curran Associates, pp. 8026–8037.
- [50] B. PEHERSTORFER, K. WILLCOX, AND M. GUNZBURGER, *Survey of multifidelity methods in uncertainty propagation, inference, and optimization*, SIAM Rev., 60 (2018), pp. 550–591, <https://doi.org/10.1137/16M1082469>.
- [51] P. PERDIKARIS, M. RAISSI, A. DAMIANOU, N. D. LAWRENCE, AND G. E. KARNIADAKIS, *Nonlinear information fusion algorithms for data-efficient multi-fidelity modelling*, Proc. R. Soc. A, 473 (2017), 20160751, <https://doi.org/10.1098/rspa.2016.0751>.
- [52] P. PERDIKARIS, D. VENTURI, J. O. ROYSET, AND G. E. KARNIADAKIS, *Multi-fidelity modelling via recursive co-kriging and Gaussian–Markov random fields*, Proc. R. Soc. A, 471 (2015), 20150018, <https://doi.org/10.1098/rspa.2015.0018>.
- [53] N. QIAN, *On the momentum term in gradient descent learning algorithms*, Neural Netw., 12 (1999), pp. 145–151, [https://doi.org/10.1016/S0893-6080\(98\)00116-6](https://doi.org/10.1016/S0893-6080(98)00116-6).
- [54] M. RAISSI, *Deep hidden physics models: Deep learning of nonlinear partial differential equations*, J. Mach. Learn. Res., 19 (2018), pp. 932–955, <https://dl.acm.org/doi/abs/10.5555/3291125.3291150>.
- [55] S. REED, A. OORD, N. KALCHBRENNER, S. G. COLMENAREJO, Z. WANG, Y. CHEN, D. BELOV, AND N. FREITAS, *Parallel multiscale autoregressive density estimation*, in Proceedings of the 34th International Conference on Machine Learning, Sydney, Australia, 2017, PMLR, pp. 2912–2921.
- [56] O. RUSSAKOVSKY, J. DENG, H. SU, J. KRAUSE, S. SATHEESH, S. MA, Z. HUANG, A. KARPATY, A. KHOSLA, M. BERNSTEIN, A. C. BERG, AND F.-F. LI, *ImageNet large scale visual recognition challenge*, Int. J. Comput. Vis., 115 (2015), pp. 211–252, <https://doi.org/10.1007/s11263-015-0816-y>.
- [57] V. SINDHWANI, H. Q. MINH, AND A. C. LOZANO, *Scalable matrix-valued kernel learning for high-dimensional nonlinear multivariate regression and Granger Causality*, in Proceedings of the Twenty-Ninth Conference on Uncertainty in Artificial Intelligence, Bellevue, WA, 2013, AUAI Press, pp. 586–595.
- [58] M. SUN, X. YAN, AND R. SCLABASSI, *Solving partial differential equations in real-time using artificial neural network signal processing as an alternative to finite-element analysis*, in International Conference on Neural Networks and Signal Processing, 2003. Proceedings of the 2003, vol. 1, Nanjing, China, 2003, IEEE, pp. 381–384, <https://doi.org/10.1109/ICNNSP.2003.1279289>.
- [59] J. TOMPSON, K. SCHLACHTER, P. SPRECHMANN, AND K. PERLIN, *Accelerating Eulerian fluid simulation with convolutional networks*, in Proceedings of the 34th International Conference on Machine Learning, Sydney, Australia, 2017, PMLR, pp. 3424–3433.
- [60] Y. WANG, Q. YAO, J. T. KWOK, AND L. M. NI, *Generalizing from a few examples: A survey on few-shot learning*, ACM Comput. Surv., 53 (2020), 63, <https://doi.org/10.1145/3386252>.
- [61] D. WEINSHALL, G. COHEN, AND D. AMIR, *Curriculum learning by transfer learning: Theory and experiments with deep networks*, in Proceedings of the 35th International Conference on Machine Learning, Stockholm, Sweden, 2018, PMLR, pp. 5238–5246.
- [62] L. ZHANG, J. HAN, H. WANG, R. CAR, AND W. E, *Deep potential molecular dynamics: A scalable model with the accuracy of quantum mechanics*, Phys. Rev. Lett., 120 (2018), 143001, <https://doi.org/10.1103/PhysRevLett.120.143001>.

**SUPPLEMENTARY MATERIALS:
MULTI-LEVEL FINE-TUNING: CLOSING GENERALIZATION GAPS
IN APPROXIMATION OF SOLUTION MAPS
UNDER A LIMITED BUDGET FOR TRAINING DATA**

ZHIHAN LI , YUWEI FAN , AND LEXING YING

SM1. Proofs of theorems.

Proof of Theorem 3.3. This theorem is a generalization of the Rademacher complexity of kernel classes [SM3, SM11] to the vector-valued case [SM10, SM13].

Firstly, we observe from the independence condition $\nu_m \perp \sigma_m$ that

$$\begin{aligned}
 \hat{\mathfrak{R}}_{v,\nu}(\mathcal{B}(\hat{f}_{l-1}, D)) &= \frac{1}{M_l} \mathbb{E}_{\sigma,\nu} \sup_{\|f\|_{\mathcal{H}} \leq D} \sum_{m=1}^{M_l} \sigma_m \nu_m^\top (\hat{f}_{l-1} + f)(v_m^l) \\
 \text{(SM1.1)} \qquad \qquad \qquad &= \frac{1}{M_l} \mathbb{E}_{\sigma,\nu} \sup_{\|f\|_{\mathcal{H}} \leq D} \sum_{m=1}^{M_l} \sigma_m \nu_m^\top f(v_m^l) \\
 &= \hat{\mathfrak{R}}_{v,\nu}(\mathcal{B}(0, D)).
 \end{aligned}$$

This means that the empirical Rademacher complexity of the \mathcal{H} -ball $\mathcal{B}(\hat{f}_{l-1}, D)$ is not dependent on the center \hat{f}_{l-1} .

Moreover, we deduce

$$\begin{aligned}
 \hat{\mathfrak{R}}_{v^l,\nu}(\mathcal{B}(\hat{f}_{l-1}, D)) &= \frac{1}{M_l} \mathbb{E}_{\sigma,\nu} \sup_{\|f\|_{\mathcal{H}} \leq D} \sum_{m=1}^{M_l} \langle f, \sigma_m \Theta(\cdot, v_m^l) \nu_m \rangle_{\mathcal{H}} \\
 &= \frac{1}{M_l} \mathbb{E}_{\sigma,\nu} \sup_{\|f\|_{\mathcal{H}} \leq D} \left\langle f, \sum_{m=1}^{M_l} \sigma_m \Theta(\cdot, v_m^l) \nu_m \right\rangle_{\mathcal{H}} \\
 &= \frac{D}{M_l} \mathbb{E}_{\sigma,\nu} \left\| \sum_{m=1}^{M_l} \sigma_m \Theta(\cdot, v_m^l) \nu_m \right\|_{\mathcal{H}} \\
 \text{(SM1.2)} \qquad \qquad \qquad &\leq \frac{D}{M_l} \sqrt{\mathbb{E}_{\sigma,\nu} \left\| \sum_{m=1}^{M_l} \sigma_m \Theta(\cdot, v_m^l) \nu_m \right\|_{\mathcal{H}}^2} \\
 &= \frac{D}{M_l} \sqrt{\sum_{m=1}^{M_l} \mathbb{E}_{\nu_m} \nu_m^\top \Theta(v_m^l, v_m^l) \nu_m} \\
 &\leq \frac{DR}{\sqrt{M_l}}
 \end{aligned}$$

as desired. □

Proof of Theorem 3.4. Since we aim to approximate the level- l solver function f_l at level l , we define the loss function to be

$$\text{(SM1.3)} \qquad \qquad \ell(u; v) = \|f_l(v) - u\|_2 \wedge B_l.$$

We note the Lipschitz condition in u :

$$\text{(SM1.4)} \qquad \qquad \ell(u; v) - \ell(u'; v) \leq \|u - u'\|_2.$$

SM1

By leveraging the independence between σ_1 and $\sigma_{>1} = (\sigma_2, \sigma_3, \dots, \sigma_{M_l})$, we have

(SM1.5)

$$\begin{aligned} \hat{\mathfrak{R}}_{v^l}(\mathcal{L}(\hat{f}_{l-1}, D; f_l, B_l)) &= \frac{1}{M_l} \mathbb{E}_{\sigma} \sup_{f \in \mathcal{B}(\hat{f}_{l-1}, D)} \sum_{m=1}^{M_l} \sigma_m \ell(f(v_m^l); v_m^l) \\ &= \frac{1}{2M_l} \mathbb{E}_{\sigma_{>1}} \sup_{f, f' \in \mathcal{B}(\hat{f}_{l-1}, D)} \left(\ell(f(v_1^l); v_1^l) - \ell(f'(v_1^l); v_1^l) \right. \\ &\quad \left. + \sum_{m=2}^{M_l} \sigma_m \ell(f(v_m^l); v_m^l) + \sum_{m=2}^{M_l} \sigma_m \ell(f'(v_m^l); v_m^l) \right). \end{aligned}$$

For a specific $\sigma_{>1}$, since

$$\begin{aligned} \text{(SM1.6)} \quad \ell(f(v_1^l); v_1^l) - \ell(f'(v_1^l); v_1^l) &\leq \|f(v_1^l) - f'(v_1^l)\|_2 = \sup_{\|\nu_1\|_2=1} \nu_1^\top (f(v_1^l) - f'(v_1^l)), \end{aligned}$$

we deduce

(SM1.7)

$$\begin{aligned} \hat{\mathfrak{R}}_{v^l}(\mathcal{L}(\hat{f}_{l-1}, D; f_l, B_l)) &\leq \frac{1}{2M_l} \mathbb{E}_{\sigma_{>1}} \sup_{f, f' \in \mathcal{B}(\hat{f}_{l-1}, D)} \sup_{\|\nu_1\|_2=1} \left(\nu_1^\top f(v_1^l) - \nu_1^\top f'(v_1^l) \right. \\ &\quad \left. + \sum_{m=2}^{M_l} \sigma_m \ell(f(v_m^l); v_m^l) + \sum_{m=2}^{M_l} \sigma_m \ell(f'(v_m^l); v_m^l) \right) \\ &= \frac{1}{M_l} \sup_{\substack{\|\nu_1\|_2 \equiv 1 \\ \nu_1 \perp \sigma_1}} \mathbb{E}_{\sigma, \nu_1} \sup_{f \in \mathcal{B}(\hat{f}_{l-1}, D)} \left(\sigma_1 \nu_1^\top f(v_1^l) \right. \\ &\quad \left. + \sum_{m=2}^{M_l} \sigma_m \ell(f(v_m^l); v_m^l) \right). \end{aligned}$$

Here the second supremum on ν_1 is taken over all random vectors ν_1 satisfying the normalization condition $\|\nu_1\|_2 \equiv 1$ and the independence condition $\nu_1 \perp \sigma_1$. This is because in the first supremum (SM1.6) ν_1 only depends on $\sigma_{>1}$ but not σ_1 .

By repeating this process, we deduce

$$\begin{aligned} \hat{\mathfrak{R}}_{v^l}(\mathcal{L}(\hat{f}_{l-1}, D; f_l, B_l)) &\leq \frac{1}{M_l} \sup_{\substack{\|\nu_m\| \equiv 1 \\ \nu_m \perp \sigma_m}} \mathbb{E}_{\sigma, \nu} \sup_{f \in \mathcal{B}(\hat{f}_{l-1}, D)} \sum_{m=1}^{M_l} \sigma_m \nu_m^\top f(v_m^l) \\ \text{(SM1.8)} \quad &\leq \sup_{\substack{\|\nu_m\| \equiv 1 \\ \nu_m \perp \sigma_m}} \hat{\mathfrak{R}}_{v^l, \nu}(\mathcal{B}(\hat{f}_{l-1}, D)) \\ &\leq \frac{DR}{\sqrt{M_l}}, \end{aligned}$$

where the last inequality follows from [Theorem 3.3](#). \square

Proof of Theorem 3.5. Since $\|\hat{f}_l - \hat{f}_{l-1}\|_{\mathcal{H}} = \|\mathbf{f}_l(\mathbf{v}^l) - \hat{\mathbf{f}}_{l-1}(\mathbf{v}^l)\|_{\mathbf{G}_l^{-1}}$ depends on the random training samples $\{(v_m^l, u_m^l)\}_{m=1}^{M_l}$, we cannot directly assume a hypothesis space $\mathcal{B}(\hat{f}_{l-1}, D)$ where D is a deterministic constant.

We use the technique exploited in [SM1]. Since by Theorem 3.1

$$(SM1.9) \quad \|\hat{f}_l - \hat{f}_{l-1}\|_{\mathcal{H}} = \|\mathbb{P}_{\mathcal{M}_l}(f_l - \hat{f}_{l-1})\|_{\mathcal{H}} \leq \|f_l - \hat{f}_{l-1}\|_{\mathcal{H}},$$

where the right hand side is known before random samples are generated, we may cover the possible hypothesis space by several \mathcal{H} -balls.

In detail, we assume $\lceil \|f_l - \hat{f}_{l-1}\|_{\mathcal{H}}/B_l \rceil = K_l$. Hence, by applying Theorem 1.1 for K_l times, with probability $1 - \delta$ on generating training samples $\{(v_m^l, u_m^l)\}_{m=1}^{M_l}$, for all $1 \leq k \leq K_l$ it holds that

$$(SM1.10) \quad \sup_{\substack{f \in \mathcal{B}(\hat{f}_{l-1}, kB_l) \\ f(v_m^l) = f_l(v_m^l)}} \mathbb{E}_{v^l \sim \mathcal{D}} (\|f_l(v^l) - f(v^l)\|_2 \wedge B_l) \\ \leq 2\hat{\mathfrak{R}}_{v^l}(\mathcal{L}(\hat{f}_{l-1}, kB_l; f_l, B_l)) + 3B_l \sqrt{\frac{\log K_l/\delta}{2M_l}}.$$

For a specific set of training samples $\{(v_m^l, u_m^l)\}_{m=1}^{M_l}$, (SM1.9) guarantees the existence of k_0 such that $1 \leq k_0 \leq K_l$ and

$$(SM1.11) \quad (k_0 - 1)B_l \leq \|\hat{f}_l - \hat{f}_{l-1}\|_{\mathcal{H}} \leq k_0 B_l.$$

As a result, $\hat{f}_l \in \mathcal{B}(\hat{f}_{l-1}, k_0 B_l)$. Since by Theorem 3.1 $\hat{f}_l(v_m^l) = f_l(v_m^l)$, (SM1.10) can be applied to $f = \hat{f}_l$ with $k = k_0$. In this case,

$$(SM1.12) \quad \hat{\mathfrak{R}}_{v^l}(\mathcal{L}(\hat{f}_{l-1}, k_0 B_l; f_l, B_l)) \leq \frac{k_0 B_l R}{\sqrt{M_l}} \leq \frac{R \|\hat{f}_l - \hat{f}_{l-1}\|_{\mathcal{H}}}{\sqrt{M_l}} + \frac{B_l R}{\sqrt{M_l}}.$$

Plugging (SM1.12) into (SM1.10), we obtain

$$(SM1.13) \quad \mathbb{E}_{v^l \sim \mathcal{D}} (\|f_l(v^l) - \hat{f}_l(v^l)\|_2 \wedge B) \leq \frac{2R \|\hat{f}_l - \hat{f}_{l-1}\|_{\mathcal{H}}}{\sqrt{M_l}} + \frac{2B_l R}{\sqrt{M_l}} + 3B_l \sqrt{\frac{\log K_l/\delta}{2M_l}}$$

as desired. \square

SM2. Model specification.

SM2.1. MNN- \mathcal{H} network. In the numerical experiments, we mainly use the MNN- \mathcal{H} network [SM7]. Since we are tackling problems with discontinuities, dilated convolution [SM14] is not applicable because it may introduce greater jumps by sub-sampling with strides. We make some adaptations to the MNN- \mathcal{H} architecture for our numerical experiments.

We describe different branches of the MNN- \mathcal{H} network by the number of nodes. For example, for a one-dimensional MNN- \mathcal{H} network, the branch of 40 nodes has intermediate activations of shape [batch_size, 40]. We leave out the adjacent component $A^{(\text{ad})}$ specified in [SM7] because it is covered by other branches.

We enlarge the restriction and interpolation maps, namely LCR and LCI layers in [SM7] to convolutional layers whose window sizes are larger than one. We also initialize these layers with preset numerical restriction and interpolation operators. This technique is found to stabilize the training and increase the accuracy.

We use the Neural Tangent Kernel (NTK) parameterization [SM8], which scales the output (activation) or each layer by $1/\sqrt{C}$ where C is the number of channels in

the layer. Except for manually initialized layers, parameters (weights and biases) of other layers are initialized independently using the unit Gaussian $\mathcal{N}(0, 1)$. We always set the scaling coefficients for weights and biases to 1 (β in [SM8] and `W_std`, `b_std` in [SM12]). We describe the parameterization and initialization of LCR and LCI layers. We take the case of one dimension as an example. We assume the spatial dimension of input to be $N = N_L$, or equivalently the shape of input of the neural network to be `[batch_size, N]`. We consider the branch with N_{sub} nodes. Weights of the LCR layer are initialized as

$$(SM2.1) \quad W_{cdw} = \sqrt{\frac{C}{N/N_{\text{sub}}}} W_c R_{dw},$$

where $1 \leq c \leq C$ is for output channels, $1 \leq d \leq N/N_{\text{sub}}$ is for input channels, and $-W \leq w \leq W$ is for the window of convolution. Here R_{dw} is a numerical restriction operator with normalization condition $\sum_{d=1}^{N/N_{\text{sub}}} \sum_{w=-W}^W R_{dw} = 1$. At initialization, we sample W_c independently from $\mathcal{N}(0, 1)$ for $1 \leq c \leq C$. Weights of the LCI layer are initialized as

$$(SM2.2) \quad W_{dcw} = \sqrt{\frac{C}{N/N_{\text{sub}}}} W_c I_{dw},$$

where $1 \leq c \leq C$ is for input channels, $1 \leq d \leq N/N_{\text{sub}}$ is for output channels, and $-W \leq w \leq W$ is for the window. Here I_{dw} is a numerical interpolation operator with normalization condition $\sum_{w=-W}^W I_{dw} = 1$. At initialization, we sample W_c independently from $\mathcal{N}(0, 1)$ for $1 \leq c \leq C$. Biases of the LCR and LCI layers are sampled from $\mathcal{N}(0, 1)$ independently for initialization.

In order to remove the randomness in computing $c_1 = \|\mathbf{f}_1(\mathbf{v}^1) - \hat{\mathbf{f}}_0(\mathbf{v}^1)\|_{\mathbf{G}_1^{-1}}$ in [subsection 3.3](#), we scale the output of neural network by a small constant γ . In this way, we have $\hat{f}_0(v_m^1) \approx 0$ and we are able to compute $c_1 \approx \|\mathbf{f}_1(\mathbf{v}^1)\|_{\mathbf{G}_1^{-1}}$ regardless of random initialization of the network. We note that γ is not permitted to be too small, or otherwise the back-propagation gradients diminish. We do not intend to bring the network into the lazy training regime by introduce this scaling as in [SM6]. Actually, the scaling $1/\sqrt{C}$ in NTK parameterization already results in lazy training. For visualization, we plot the output of neural network at initialization in [Figure SM1](#).

SM2.2. Models for experiments. For the non-linear Schrödinger equation problem, we use a one-dimensional MNN- \mathcal{H} network with spatial dimension of input $N = 320$. We deploy 6 branches with the number of nodes $N_{\text{sub}} = 10, 20, 40, 80, 160$, and 320 respectively. The numbers of layers and channels of each branch are 5 and 160 respectively. We initialize the LCR layer with average operator and the LCI layer with linear interpolation operator. The window size is 3 for LCR and LCI layers and 7 for intermediate convolutional layers. The scaling constant is $\gamma = 3.0 \times 10^{-4}$.

For the viscous Burgers' equation problem, we cast a Convolution Neural Network (CNN) as a one-dimensional MNN- \mathcal{H} network with spatial dimension of input $N = 320$. As a CNN, we deploy only 1 branch with the number of nodes $N_{\text{sub}} = 320$. There are 9 layers and 160 channels in the network. We initialize the LCR layer with average operator and the LCI layer with linear interpolation operator. The window size is 3 for LCR and LCI layers and 15 for intermediate convolutional layers. The scaling constant is $\gamma = 3.0 \times 10^{-2}$.

For the diagonal of inverse problem, we use a two-dimensional MNN- \mathcal{H} network with spatial dimension of input $N \times N = 80 \times 80$. We deploy 4 branches with the

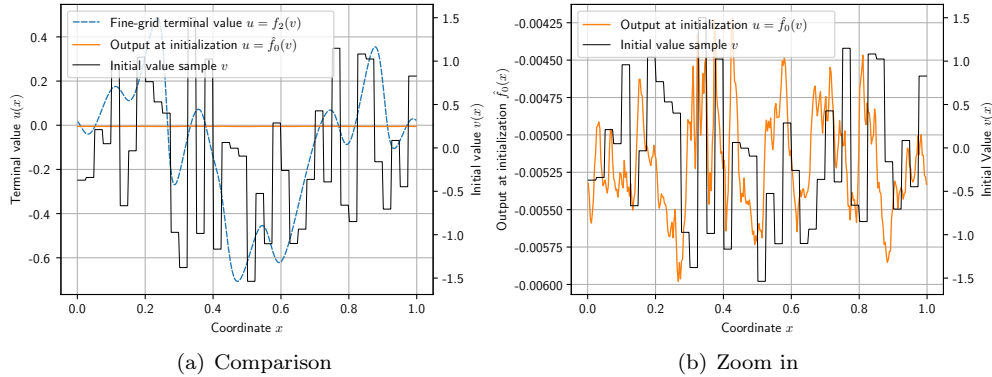


FIG. SM1. Visualization of the output of neural network at initialization for the viscous Burgers' equation problem. We note that from (a) the output at initialization $f_0^0(v)$ nearly vanishes compared to the solution given by the fine-grid solver $f_2(v)$. However, from (b) it does not really vanish so the back-propagation gradients do not diminish.

number of nodes $N_{\text{sub}} \times N_{\text{sub}} = 10 \times 10, 20 \times 20, 40 \times 40$ and 80×80 respectively. The numbers of layers and channels of each branch are 3 and 40 respectively. We initialize the LCR layer with average operator and the LCI layer with linear interpolation operator. The window size is 3×3 for LCR and LCI layers and 7×7 for intermediate convolutional layers. The scaling constant is $\gamma = 1.0 \times 10^{-3}$.

SM3. Problem specification.

SM3.1. Computation time. We measure the time t_l to generate training samples at different levels. For each problem in section 4, we generate $M = 16384$ training samples with 6 cores in parallel on Intel Xeon CPU E5-2690. We vary the grid step $h = 1/N$ and measure the CPU time for generating training samples. The results are shown in Figure SM2. We note that the grid is of size N for one-dimensional problems (the non-linear Schrödinger equation problem and the viscous Burgers' equation problem), and of size $N \times N$ for two-dimensional problems (the diagonal of inverse problem).

According to the measurements, we are able to justify the following relationships between t_l , which are critical to the budget distribution problem (1.6). For the non-linear Schrödinger equation problem, we set $t_2 = 64t_1$ as observed in Figure SM2. For the viscous Burgers' equation problem, we set $t_2 = 64t_1$ according to the scaling law in time. For the diagonal of inverse problem, we set $t_4 = 8t_3 = 64t_2 = 512t_1$ according to the scaling law in time.

SM3.2. Pre-processing. We perform pre-processing on the generated training samples before we fit regression networks on the samples. Pre-processing procedures are done for most machine learning algorithms (e.g., normalization, whitening, or centering).

For the non-linear Schrödinger equation problem, we observe that when the potential $v(x) \equiv 0$ the corresponding ground state is $u(x) \equiv 1$. To center the ground states, we record $u_m^l - 1 = f_l(v_m^l) - 1$ instead of u_m^l for the training sample pairs.

We do not perform pre-processing on the training samples for the viscous Burgers' equation problem.

For the diagonal of inverse problem, we notice that the potential (4.4) has expected

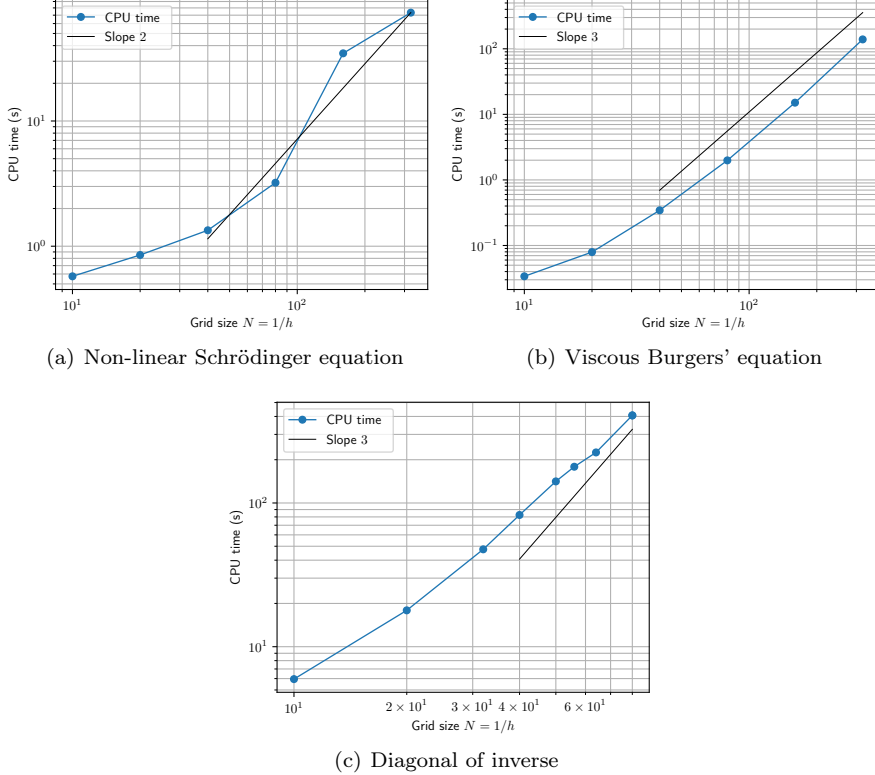


FIG. SM2. Measured CPU time in generating $M = 16384$ training samples at different grid steps. For the non-linear Schrödinger equation problem, we observe a rapid increment of computation time for $80 \leq N \leq 160$. This is caused by the high-frequency oscillations (4.1) which are only visible on fine grids and hinder the convergence of the gradient flow solver. For the viscous Burgers' equation problem we observe a scaling of order $O(1/h^3)$. For the diagonal of inverse problem, we also observe a scaling of order $O(1/h^3)$ as given in [SM9].

tation $E v^l(x, y) \equiv C$. To center the potentials, we record $v_m^l - C$ instead of v_m^l for the training samples pairs. Since the two-dimensional Green function has singularities of logarithmic growth near the diagonal, further numerical treatment is required to match solutions generated at different grids. We find from Fourier analysis that when the potential $v^l(x, y) \equiv C$, the diagonal of inverse to the discretized Schrödinger operator on the $N_l \times N_l$ grid Ω_l is

$$(SM3.1) \quad u^l(x, y) \equiv \tilde{C}_l = \sum_{i=1}^{N_l} \sum_{j=1}^{N_l} \frac{1}{4N_l^2 (\sin^2 i\pi/N_l + \sin^2 j\pi/N_l) + C}.$$

To center the diagonal of inverses, we record $u_m^l - \tilde{C}_l = f_l(v_m^l) - \tilde{C}_l$ for the training sample pairs when the grid step is $h_l = 1/N_l$.

SM4. Neural Tangent Kernel.

SM4.1. Computation. The computation of Conjugate Kernel (CK) and NTK of infinite-width networks has been extensively studied and efficiently implemented [SM8, SM2]. We use the Neural Tangents package [SM12] together with JAX [SM4]

and Stax [SM5] to compute the NTK. Since the infinite-width NTK can be computed by sequentially applying CK and NTK operations corresponding to the layers [SM12], we only need to specify the CK and NTK operations of manually initialized LCR and LCI layers introduce in subsection SM2.1.

For LCR layers, the initialization (SM2.1) can be recognized as restricting the input as a function on $N \times N$ grid to $N_{\text{sub}} \times N_{\text{sub}}$ grid with the restriction operator R and then randomizing over channels. As a result, the CK Σ of a LCR layer is the inner product kernel of restricted functions, namely

(SM4.1)

$$\Sigma_{nn'}(v, v') = \frac{1}{(2W+1)(N/N_{\text{sub}})} \sum_{w=-W}^W \sum_{w'=-W}^W \sum_{d=1}^{N/N_{\text{sub}}} \sum_{d'=1}^{N/N_{\text{sub}}} R_{dw} R_{d'w'} v_{nd} v'_{n'd'} + 1,$$

where $1 \leq n, n' \leq N_{\text{sub}}$ are for spatial dimension and v, v' are recognized as shape $N_{\text{sub}} \times (N/N_{\text{sub}})$ by reshaping the tensor. The NTK of a manually initialized LCR layer is identical to a randomly initialized one, which turns out to be a standard convolutional layer.

For LCI layers, the CK Σ is obtained by conjugating the CK Σ' from the previous layer by the interpolation operator I as

$$(SM4.2) \quad \Sigma_{nn'dd'}(v, v') = \frac{1}{2W+1} \sum_{w=-W}^W \sum_{w'=-W}^W I_{dw} I_{d'w'} \Sigma'_{(n+w)(n'+w')}(v, v') + \delta_{dd'},$$

where $1 \leq n, n' \leq N_{\text{sub}}$ are for spatial dimension, $1 \leq d, d' \leq N/N_{\text{sub}}$ are for output channels, and $\delta_{dd'}$ is the Kronecker delta. The NTK Θ is also obtained by Σ' and the NTK from the previous layer Θ'

$$(SM4.3) \quad \Theta_{nn'dd'}(v, v') = \frac{1}{2W+1} \sum_{w=-W}^W \sum_{w'=-W}^W I_{dw} I_{d'w'} \Theta'_{(n+w)(n'+w')}(v, v') \\ + \delta_{dd'} + \frac{1}{2W+1} \sum_{w=-W}^W \Sigma'_{(n+w)(n'+w')}(v, v') \delta_{dd'},$$

where $1 \leq n, n' \leq N_{\text{sub}}$ are for spatial dimension and $1 \leq d, d' \leq N/N_{\text{sub}}$ are for output channels. The CK Σ and NTK Θ above are of shape $N_{\text{sub}} \times N_{\text{sub}} \times (N/N_{\text{sub}}) \times (N/N_{\text{sub}})$, which can be recognized as shape $(N_{\text{sub}} \times N/N_{\text{sub}}) \times (N_{\text{sub}} \times N/N_{\text{sub}}) = N \times N$ by reshaping the tensor.

SM4.2. Convergence of Neural Tangent Kernel. We study the convergence of NTK in the example of non-linear Schrödinger equation. We use the Neural Tangents package [SM12] to compute the infinite-width NTK Θ_{∞} . Meanwhile, we can also use the package to compute the NTK of finite-width networks according to (3.3) directly. We consider the NTK Θ_0 of finite-width network at initialization, namely the NTK of \hat{f}_0 . We also consider finite-width NTK Θ_1 of \hat{f}_1 after the first level of training with $M_1 = 1024$ coarse-grid samples and Θ_2 of \hat{f}_2 after two levels of training, fine-tuned with $M_2 = 16$ fine-grid samples starting from \hat{f}_1 . We sample four $v_m \sim \mathcal{D}$ for $1 \leq m \leq 4$, and show the corresponding NTK $\Theta_{\infty}(v_1, v_m)$, $\Theta_0(v_1, v_m)$, $\Theta_1(v_1, v_m)$, and $\Theta_2(v_1, v_m)$ in Figure SM3. We note that since the output of the network is multi-dimensional, the NTK is a matrix-valued kernel.

Since the training process turns out to be kernel “ridgeless” regression in the NTK regime [SM8], we are particular interested in the RKHS norm $\|\hat{f}_1 - \hat{f}_0\|_{\mathcal{H}}$

$\|\mathbf{f}_1(\mathbf{v}^1) - \hat{\mathbf{f}}_0(\mathbf{v}^1)\|_{\mathbf{G}_1^{-1}} \approx \|\mathbf{f}_1(\mathbf{v}^1)\|_{\mathbf{G}_1^{-1}}$ and $\|\hat{\mathbf{f}}_2 - \hat{\mathbf{f}}_1\|_{\mathcal{H}} = \|\mathbf{f}_2(\mathbf{v}^2) - \hat{\mathbf{f}}_1(\mathbf{v}^2)\|_{\mathbf{G}_2^{-1}}$ in \mathcal{H} induced by the NTK. For $M = 16$ samples $\{v_m\}_{m=1}^M$, we compute the RKHS norm $\|\mathbf{f}_1(\mathbf{v})\|_{\mathbf{G}^{-1}}$ with infinite-width NTK Θ_∞ and finite-width NTK Θ_0, Θ_1 for the Gram matrix \mathbf{G} of $\{v_m\}_{m=1}^M$. We also compute the RKHS norm $\|\mathbf{f}_2(\mathbf{v}) - \hat{\mathbf{f}}_1(\mathbf{v})\|_{\mathbf{G}^{-1}}$ with finite-width NTK Θ_1 and Θ_2 . We draw 64 collections of samples $\{v_m\}_{m=1}^M$ by $v_m \sim \mathcal{D}$ independently and study the correlation between RKHS norms with $\Theta_\infty, \Theta_0, \Theta_1$, and Θ_2 in Figure SM4.

SM4.3. Growth of coefficients c_l and d_l . We introduce the coefficients c_l for $1 \leq l \leq L$ and d_l for $2 \leq l \leq L$ to construct the *a priori* error estimator in subsection 3.3. According to (3.19) and (3.24), computing c_l and d_l involves computing the Gram matrix \mathbf{G}_l and its inverse. However, we note that the Gram matrix is of size $M_l N_L^d \times M_l N_L^d$, which becomes prohibitively huge when M_l becomes large. For example, we can only compute the Gram matrix with $M_l = 24$ samples at a time on Nvidia Tesla K80 for the non-linear Schrödinger equation problem where $N_L = 320$ and $d = 1$. As a result, we only use 16 samples instead of M_l samples when computing the RKHS norms in Figures 7 and 8. In this way, the linear correlation shown in Figure 7 shows the convergence of the generalization error g_1 in speed $O(1/\sqrt{M_1})$.

We study the growth of the coefficients c_l and d_l with respect to the number of training samples M_l . We still take the non-linear Schrödinger equation as an example. For computing the Gram matrix with more samples, we consider a smaller problem: we use the coarse grid with grid step $h_1 = 1/N_1 = 1/20$ and the fine grid with grid step $h_2 = 1/N_2 = 1/40$ respectively. We still use (4.1) for the distribution \mathcal{D} of potential v but set $K = 4$ and sample $A_k \sim \mathcal{U}[-400, -200]$, $\omega_k \sim \mathcal{U}[8, 16]$, $1/\sigma_k \sim \mathcal{U}[4, 8]$, and $\phi_k \sim \mathcal{U}[0, 2\pi]$ independently. Besides the growth of $c_1 = \|\mathbf{f}_1(\mathbf{v}^1)\|_{\mathbf{G}_1^{-1}}$ with respect to M_1 , since by (3.24)

$$(SM4.4) \quad \hat{g}_2 = \frac{2Rc_2}{\sqrt{M_2}} \left(1 + \frac{d_2 \hat{g}_1}{c_2^2} \right),$$

we study the growth of $d_2/c_2^2 = M_2 \|\mathbf{G}_2^{-1}(\mathbf{f}_2(\mathbf{v}^2) - \mathbf{f}_1(\mathbf{v}^2))\|_{2,\infty} / \|\mathbf{f}_2(\mathbf{v}^2) - \mathbf{f}_1(\mathbf{v}^2)\|_{\mathbf{G}_2^{-1}}^2$ with respect to M_2 . The growth curves are presented in Figure SM5. We observe that the growth of c_1 and d_2/c_2^2 with respect to M_1 and M_2 respectively approximately follows the power law. Due to the presence of growth exponents, it is possible to introduce exponent corrections for the *a posteriori* error estimator.

REFERENCES

- [SM1] S. ARORA, S. DU, W. HU, Z. LI, AND R. WANG, *Fine-grained analysis of optimization and generalization for overparameterized two-layer neural networks*, in Proceedings of the 36th International Conference on Machine Learning, Long Beach, CA, 2019, PMLR, pp. 322–332.
- [SM2] S. ARORA, S. S. DU, W. HU, Z. LI, R. R. SALAKHUTDINOV, AND R. WANG, *On Exact Computation with an Infinitely Wide Neural Net*, in Advances in Neural Information Processing Systems, vol. 32, Vancouver, Canada, 2019, Curran Associates, pp. 8141–8150.
- [SM3] P. L. BARTLETT AND S. MENDELSON, *Rademacher and Gaussian complexities: Risk bounds and structural results*, in Computational Learning Theory. COLT 2001. Lecture Notes in Computer Science, vol. 2111, Amsterdam, The Netherlands, 2001, Springer, Berlin, Heidelberg, pp. 224–240, https://doi.org/10.1007/3-540-44581-1_15.
- [SM4] J. BRADBURY, R. FROSTIG, P. HAWKINS, M. J. JOHNSON, C. LEARY, D. MACLAURIN, G. NECULA, A. PASZKE, J. VANDERPLAS, S. WANDERMAN-MILNE, AND Q. ZHANG, *JAX: composable transformations of Python+NumPy programs*, 2018, <http://github.com/google/jax>.

- [SM5] J. BRADBURY, R. FROSTIG, P. HAWKINS, M. J. JOHNSON, C. LEARY, D. MACLAURIN, G. NECULA, A. PASZKE, J. VANDERPLAS, S. WANDERMAN-MILNE, AND Q. ZHANG, *Stax, a flexible neural net specification library in JAX*, 2018, <https://github.com/google/jax/blob/master/jax/experimental/stax.py>.
- [SM6] L. CHIZAT, E. OYALLON, AND F. BACH, *On lazy training in differentiable programming*, in Advances in Neural Information Processing Systems, vol. 32, Vancouver, Canada, 2019, Curran Associates, pp. 2937–2947.
- [SM7] Y. FAN, J. FELIU-FABÀ, L. LIN, L. YING, AND L. ZEPEDA-NÚÑEZ, *A multiscale neural network based on hierarchical nested bases*, Res. Math. Sci., 6 (2019), 21, <https://doi.org/10.1007/s40687-019-0183-3>.
- [SM8] A. JACOT, F. GABRIEL, AND C. HONGLER, *Neural Tangent Kernel: Convergence and generalization in neural networks*, in Advances in Neural Information Processing Systems, vol. 31, Montreal, Canada, 2018, Curran Associates, pp. 8571–8580.
- [SM9] L. LIN, J. LU, L. YING, R. CAR, AND W. E, *Fast algorithm for extracting the diagonal of the inverse matrix with application to the electronic structure analysis of metallic systems*, Commun. Math. Sci., 7 (2009), pp. 755–777.
- [SM10] A. MAURER, *The Rademacher complexity of linear transformation classes*, in Learning Theory. COLT 2006. Lecture Notes in Computer Science, vol. 4005, Pittsburgh, PA, 2006, Springer, Berlin, Heidelberg, pp. 65–78, https://doi.org/10.1007/11776420_8.
- [SM11] M. MOHRI, A. ROSTAMIZADEH, AND A. TALWALKAR, *Foundations of machine learning*, MIT Press, Cambridge, MA, 2 ed., 2018.
- [SM12] R. NOVAK, L. XIAO, J. HRON, J. LEE, A. A. ALEMI, J. SOHL-DICKSTEIN, AND S. S. SCHOENHOLZ, *Neural Tangents: Fast and easy infinite neural networks in Python*, in 8th International Conference on Learning Representations, ICLR 2020, Addis Ababa, Ethiopia, 2020, <https://openreview.net/forum?id=SkID9yrFPS>.
- [SM13] V. SINDHWANI, H. Q. MINH, AND A. C. LOZANO, *Scalable matrix-valued kernel learning for high-dimensional nonlinear multivariate regression and Granger Causality*, in Proceedings of the Twenty-Ninth Conference on Uncertainty in Artificial Intelligence, Bellevue, WA, 2013, AUAI Press, pp. 586–595.
- [SM14] F. YU AND V. KOLTUN, *Multi-scale context aggregation by dilated convolutions*, in 4th International Conference on Learning Representations, ICLR 2016, Conference Track Proceedings, San Juan, Puerto Rico, 2016, <http://arxiv.org/abs/1511.07122>.

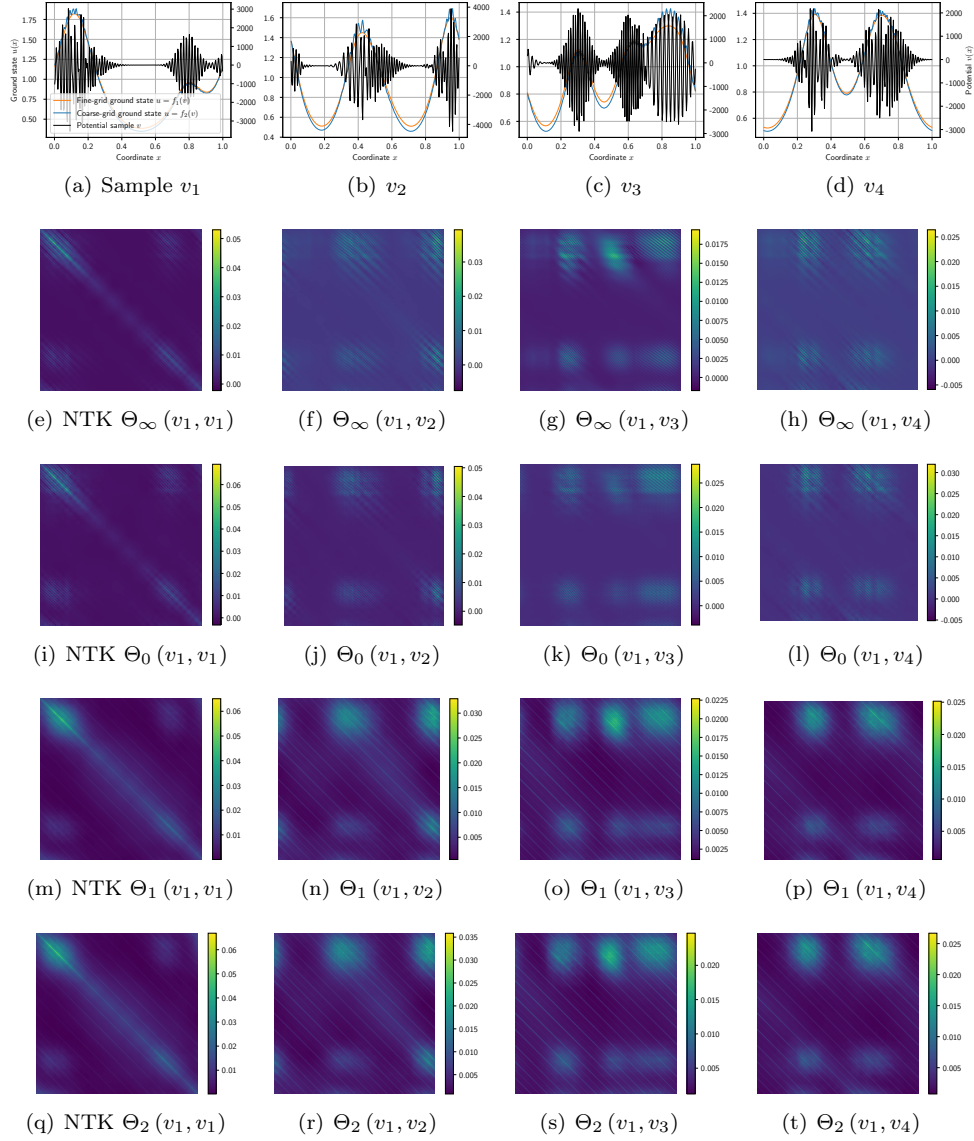


FIG. SM3. Visualization of NTK for the non-linear Schrödinger equation problem. We plot the potential samples v_m in (a-d), show infinite-width NTK $\Theta_\infty(v_1, v_m)$ in (e-h), and show finite-width NTK at initialization $\Theta_0(v_1, v_m)$ in (i-l). We also show finite-width NTK after one level of training $\Theta_1(v_1, v_m)$ in (m-p) and after two levels of training $\Theta_2(v_1, v_m)$ in (q-t). We observe that finite-width NTK at initialization Θ_0 is a qualitatively good approximation to infinite-width NTK. Although finite-width NTK changes during the first level of training from Θ_0 to Θ_1 , it still qualitatively captures prominent features of the input. We observe that finite-width NTK does not change much during the second level of fine-tuning from Θ_1 to Θ_2 .

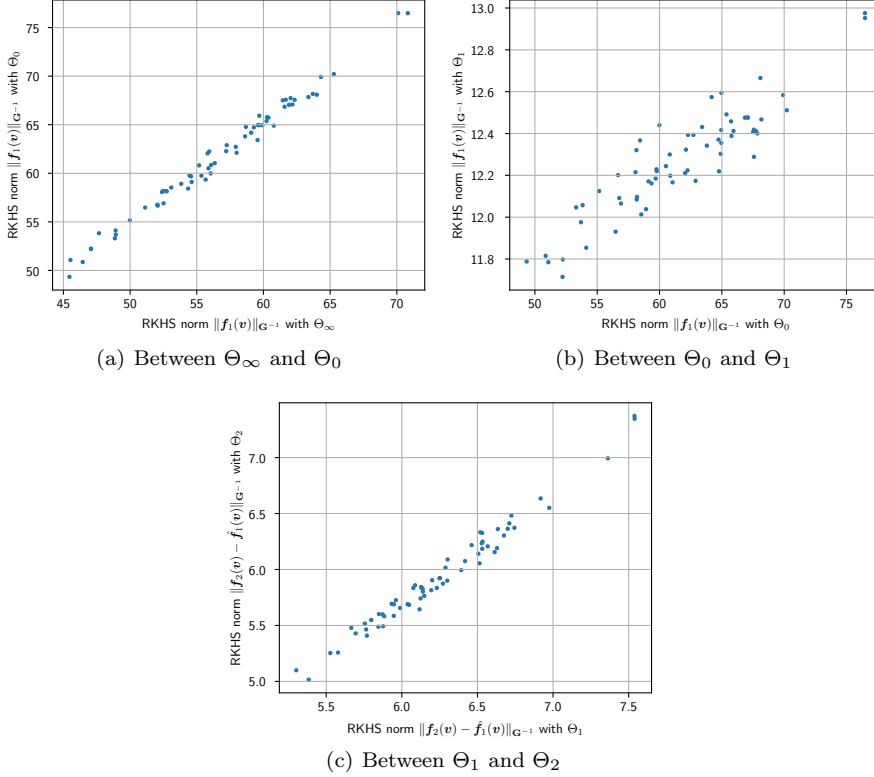


FIG. SM4. Correlation between RKHS norms $\|\mathbf{f}_1(\mathbf{v})\|_{\mathbf{G}_{-1}}$ computed with infinite-width NTK Θ_∞ and finite-width NTK Θ_0 , Θ_1 , and correlation between RKHS norms $\|\mathbf{f}_2(\mathbf{v}) - \hat{\mathbf{f}}_1(\mathbf{v})\|_{\mathbf{G}_{-1}}$ computed with finite-width NTK Θ_1 and Θ_2 . We observe a strong correlation between the RKHS norms with Θ_∞ and Θ_0 , which supports the convergence of NTK. Although the RKHS norm with Θ_1 changes in magnitude compared to Θ_0 , we still observe a linear correlation, which supports the construction of a posteriori error estimator. We again observe a strong correlation between the RKHS norms with Θ_1 and Θ_2 , which supports the validity of NTK analysis in the fine-tuning steps.

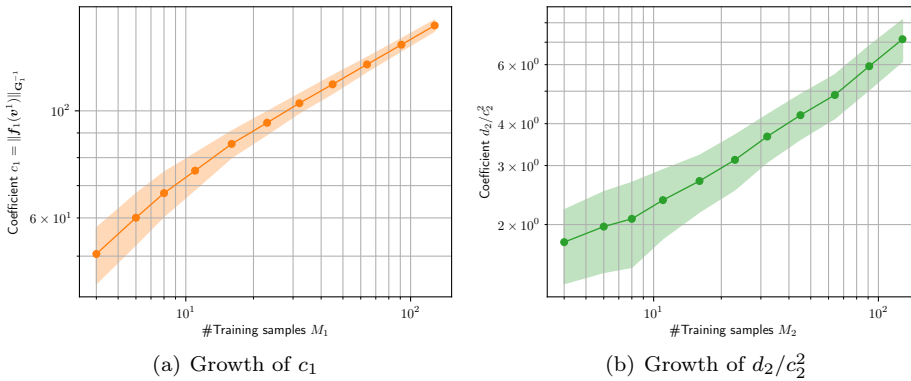


FIG. SM5. Growth of c_1 and d_2/c_2^2 with respect to M_1 and M_2 respectively. We observe that the growth of c_1 and d_2/c_2^2 are relatively slow. The slope of c_1 with respect to M_1 in (a) is $0.30588 < 1/2$, and the slope of d_2/c_2^2 with respect to M_2 in (b) is $0.40594 < 1$. As a result, the growth exponents do not qualitatively change our result. We generate 64 collections of samples, and the shaded area corresponds to the variance.